Clean Energy, 2024, Vol. 8, No. 2, 217–238
https://doi.org/10.1093/ce/zkad093
Advance access publication 26 March 2024
Review Article

A review of recent advances of kesterite thin films based on magnesium, iron and nickel for photovoltaic application: insights into synthesis, characterization and optoelectronic properties

Nelson Mauricio Espinel Pérez[1,2,*], Enrique Vera López[1], Jairo Alberto Gómez Cuaspud[1] and Juan Bautista Carda Castelló[3]

[1]Grupo de Investigación en Integridad y Evaluación de Materiales (GIEM). Instituto para la Investigación e Innovación en Ciencia y Tecnología de Materiales (INCITEMA). Universidad Pedagógica y Tecnológica de Colombia, Av. Central del Norte 39-115. Tunja–Boyacá, Colombia
[2]Servicio Nacional de Aprendizaje (Sena). Centro Minero. Vereda Morcá Sector Batá. Sogamoso–Boyacá, Colombia
[3]Universidad Jaume I. Grupo de Química Inorgánica y Orgánica. Castellón de la Plana, Campus del Riu Sec. Castellón de la Plana, España
[*]Corresponding author. E-mail: nelespinel@gmail.com

Abstract

This review emphasizes the recent advancements and prospects of thin-film kesterite-based photovoltaic (PV) applications using magnesium, iron and nickel. The quest for novel materials employed in solar cells has resulted in incorporating these elements into the composition of kesterite as substitutes or modifiers (dopants) for zinc. This integration has induced notable repercussions on the structural, optoelectronics and morphological properties, which are reviewed. The first section of this paper offers a comprehensive review of the general characteristics of kesterite minerals. These crucial materials exhibit a high absorption coefficient (10^4 cm^{-1}) and an optical band gap of 1.0–1.8 eV. Moreover, they are free of critical raw materials, non-toxic and sustainable. The second section depicts the substitution or modification of zinc by magnesium in kesterite. Additionally, this paper provides a comprehensive review of the quaternary and pentanary systems $Cu_2MgSn(S,Se)_4$ and $Cu_2Zn_{1-x}Mg_xSnS_4$, highlighting their advantages and drawbacks. In the last section, a review of the quaternary or pentanary systems is conducted, namely $Cu_2Zn_xFe_{1-x}SnS_4$ and $Cu_2Zn_xNi_{1-x}SnS_4$, along with their effects on optoelectronic properties. In conclusion, various methods for obtaining modified or substituted kesterite materials using magnesium, iron and nickel have demonstrated sustainability, scalability for industrial production and potential candidacy as substitutes for conventional PV materials. The prospects for pentanary materials ($Cu_2Zn_{1-x}Mg_xSnS_4$, $Cu_2Zn_{1-x}Fe_xSnS_4$ and $Cu_2Zn_{1-x}Ni_xSnS_4$) are to overcome the efficiency record of kesterite reported in 2014, which was 12.6 % for $Cu_2ZnSn(S,Se)_4$, and to enhance its optoelectronic properties through synthesis conditions that comply with the principles of green chemistry.

Keywords: kesterite; thin film; magnesium; iron; nickel; substitutes or modifiers; novel materials; sustainability

Introduction

Solar energy is an abundant, safe and sustainable source that can be transformed into electrical energy using photovoltaic (PV) devices. Nonetheless, the efficient conversion of this energy by using single-junction solar cells is constrained by an upper limit defined by the Shockley–Queisser (SQ) model. The above statement indicates the presence of photons with energies exceeding the forbidden band (E_g), generating holes and free electrons upon contact with a perfect selective charge. This process results in the production of one electron for every photon that is absorbed, which contributes to the electric current [1]. According to the 2021 report on renewable energies submitted by the International Energy Agency (IEA), the global energy capacity generated from PV technology is projected to reach ~200 GW by 2026 [2], as depicted in Fig. 1a. This capacity surpasses the forecasts for other renewable energy sources, including wind, hydrothermal and biofuels.

1 PV systems based on thin films

Thin-film materials are presented as a cost-effective alternative to crystalline-silicon solar cells. This can be attributed to their direct band gap, high absorption coefficients and thin layers, which can be applied on lightweight and flexible substrates. These characteristics make thin-film solar cells compatible with straightforward production techniques [3, 4]. Fig. 1b and c depicts the characteristics of thin-film materials. Moreover, this technology can also be integrated into various applications such as building, transportation, space flight and mobile energy production, highlighting its advantage over traditional power sources [5]. Table 1 compares conventional energy (c-Si) and thin-film materials, including several physical properties.

1.1 Kesterite Cu_2ZnSnS_4 (CZTS)

The Cu_2ZnSnS_4 (CZTS) and $Cu_2ZnSnSe_4$ (CZTSe) p-type kesterite minerals are thin-film semiconductor materials that are most

Received: 26 September 2023. **Accepted:** 21 December 2023

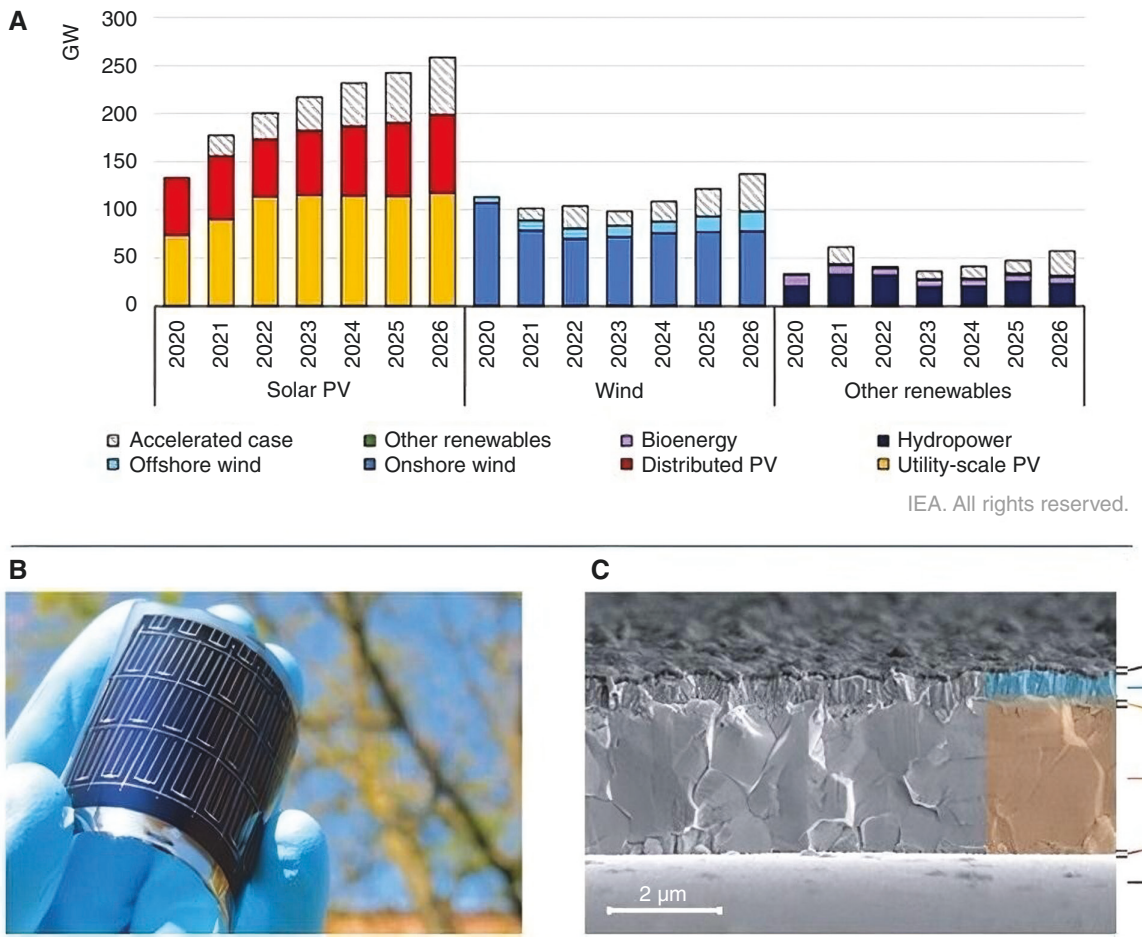

Fig. 1: (a) Annual worldwide capacity addition of photovoltaic (PV), wind and other renewables, main and accelerated cases, 2020–26 [2]; (b) CIGSe solar cell, based on polyimide substrate; (c) cross section of a scanning electron micrograph, based on polyimide substrate. (b) and (c) reproduced from [4] with permission from Elsevier.

Table 1: Comparison between conventional technology (c-Si) and thin-film materials

	c-Si	a-Si	CdTe	$Cu(In_xGa_{1-x})Se_2$ (CIGS)	Cu_2ZnSnS_4 (CZTS)	Source
Thin films	No	✓	✓	✓	✓	[6]
Absorption coefficient	2.00×10^3 cm^{-1}	1.74×10^6 cm^{-1}	1.11×10^6 cm^{-1}	$>1.00 \times 10^5$ cm^{-1}	$>1.00 \times 10^4$ cm^{-1}	[6–8].
Band gap	Indirect 1.10 eV	Direct 1.75 eV	Direct 1.44 eV	Direct 1.00–1.60 eV	Direct 1.00–1.50 eV	[6, 9, 10].
Sufficient thickness	(110–300) µm	1.00 µm	(3.00–5.00) µm	(1.00–2.00) µm	(1.00–3.00) µm	[6, 8, 11, 12]
Toxicity	None	None	Cadmium	None	None	[6–8]

promising as light absorbers for PV cells, achieving record efficiencies such as 11.6% and 12.6%, respectively [13, 14]. Due to their distinctive optical properties, such as a band-gap energy range of 1.0–1.5 eV [9] and absorption coefficients of >10^4 cm^{-1} [7], thin-film materials can be theoretically classified as ideal for electricity conversion in PV applications [15]. In addition, from a chemical and mineralogical perspective, CZTS quaternary materials are ideally constituted by 50% S, 25% Cu, 12.5% Sn and 12.5% Zn under atomic conditions. However, developing this structure introduces additional challenges due to the likelihood of forming secondary phases composed of binary or ternary sulphides, including ZnS, SnS, SnS_2, Cu_2S or Cu_2SnS_3 [16].

Similarly, secondary phases raise a significant issue because experimental and theoretical findings have revealed that the presence of kesterite can be observed within the relatively small region (indicated by the red dot) [17], as depicted in the tetrahedral phase diagrams shown in Fig. 2a and 2b [18, 19]. Additionally, the presence of secondary and ternary phases in sulphides and selenides has a more detrimental effect on solar cells, primarily due to their narrower band gap, which reduces the open-circuit voltage (V_{oc}) [22]. On the other hand, some properties and characteristics regarding the secondary and ternary phases of CZTS were identified, according to Table 2.

The secondary phases, namely CuS, Cu_2S, SnS and SnS_2, exhibit distinct crystalline structures from CZTS and can be

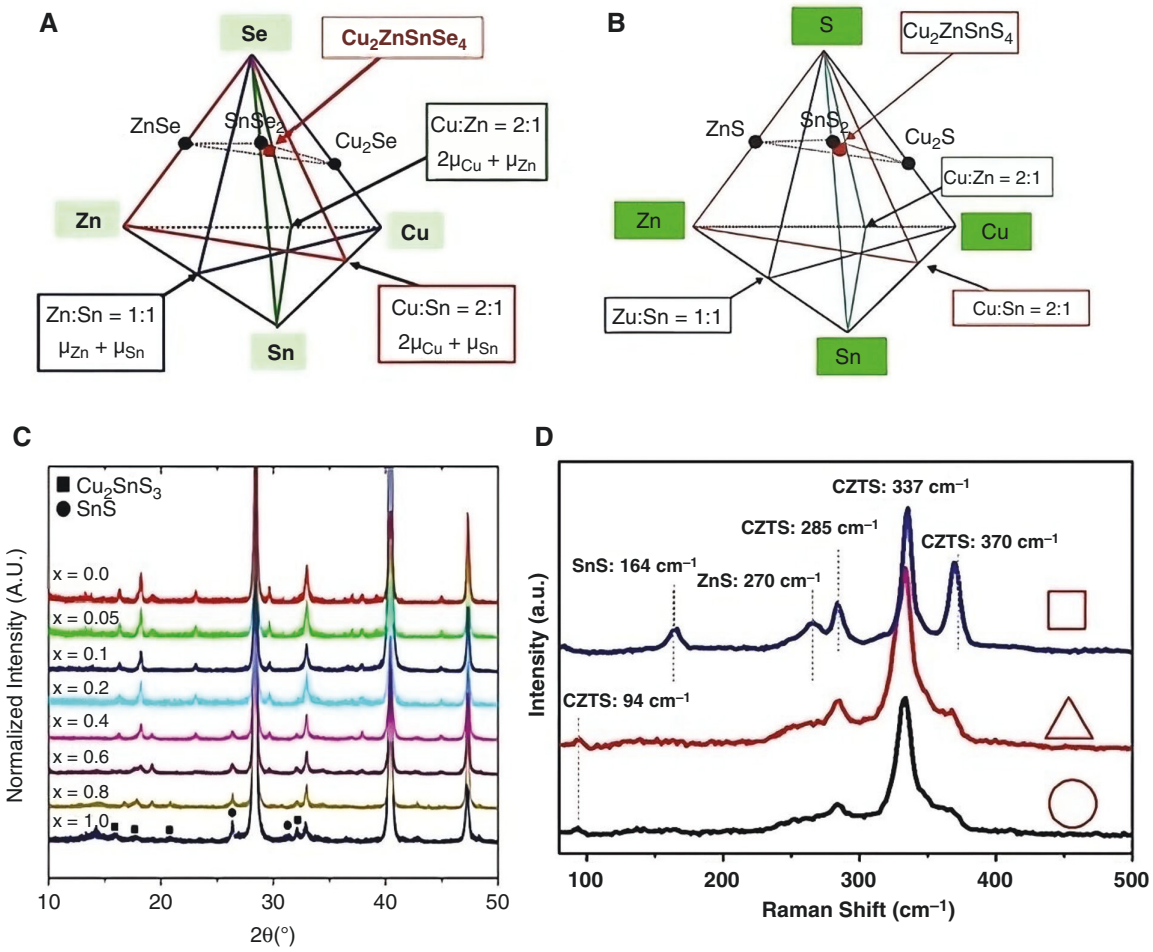

Fig. 2: (a) Schematic phase diagram of the Cu–Zn–Sn–Se quaternary system; reproduced from [18] with permission from IOP Publishing, Ltd; (b) schematic phase diagram of the Cu–Zn–Sn–S quaternary system [19]; (c) X-ray diffraction patterns for CZTS absorber layers; reproduced from [20] with permission from the American Chemical Society; (d) Raman scattering spectra for CZTS [21].

Table 2: Various properties of secondary phases observed in CZTS materials [23]

Properties	CZTS	ZnS	Cu_2S	SnS_2	Cu_2SnS_3
Band gap (eV)	1.45	3.54–3.68	1.21	2.20	0.98–1.35
Electrical properties	Semiconductor, p-type	Insulation	p-type, metal-like, highly defective	n-type	p-type
Structural properties	Kesterite	Sphalerite and wurtzite	Chalcocite	Rhombohedral	Cubic and tetragonal
Impact on solar cell performance	Essential absorbing material	Insulating, reducing device active area	Metallic, short solar cell	n-type, forms diode and barrier for carrier collection	Affects carrier collection efficiency

identified through X-ray diffraction (XRD) patterns. In contrast, the secondary-phase ZnS and the ternary-phase Cu_2SnS_3 share the same zinc-blende structure as kesterite, making them indistinguishable using the XRD technique [24]. However, Raman spectroscopy can detect these materials and identify these phases through their corresponding vibrational modes and excitation (resonant) conditions [17, 25]. Table 3 describes the Raman shift for various secondary and ternary phases at different wavelengths.

Fig. 2c showcases the unmodified (CZTS) kesterite materials. The XRD characterization technique was employed to compare its diffractograms with the XRD patterns of the Joint Committee on Powder Diffraction Standards (JCPDS) standard no. 26-0575. As a result, prominent signals were observed at the 2θ angles of 28.50°, 32.98°, 47.32° and 56.5°, concerning the crystal lattice planes [1 1 2], [2 0 0], [2 2 0] and [3 2 1], respectively [20, 21, 27]. Furthermore, the presence of the molybdenum (Mo) phase at a 2θ angle of 40.6° and potential signals of the Cu_2SnS_3 ternary phase were detected at the 2θ angles of 10.8°, 16.0°, 17.6° and 32.1°, respectively. Furthermore, there was a potential indication of the SnS phase at 2θ angles of 27.0° and 30.8°, with the JCPDS standard no. 73-1859 and JCPDS standard no. 98-10-6030

Table 3: Secondary and ternary phases observed in kesterite-type quaternary compounds, the most intense Raman signals and the optimal excitation wavelengths for their detection [26]

Secondary and ternary phases	Raman shift cm^{-1}	λ_{ex} (nm)
ZnS	350	325
Cu_2SnS_3	354, 292	532
Cu_3SnS_4	317	532
Cu_xS	475	532
SnS_2	314	532
Sn_2S_3	308	532
SnS	220, 192, 163	785
MoS_2	408	532

serving as a reference [28, 29]. On the other hand, Fig. 2d illustrates the Raman shifts obtained for CZTS, which were identified at 285, 337 and 370 cm^{-1}, respectively.

On the other hand, the electrical performance of kesterite materials has demonstrated improved results when these have a lower copper content and higher zinc content, along with specific proportions such as (Cu/Zn + Sn) = 0.8 and (Zn/Sn) = 1.2 [24], as depicted in Fig. 5a. These conditions notably influence the efficiency of the PV device when applied experimentally.

However, other factors can influence the effectiveness of the PV device, including the open-circuit voltage deficit (V_{oc}) resulting from the presence of tail bands caused by cation disorder. Furthermore, there is a significant recombination of interfaces [30]. Additionally, some authors have reported an increase in series resistances due to the undesirable formation of $MoSe_2$ between the absorber layer and the back contact, leading to a decrease in PV device efficiencies [25, 31]. Moreover, the efficiency of PV devices is significantly influenced by the heterojunction formed within the region connecting the absorber layer and the buffer layer Cu_2ZnSnS_4/CdS (CZTS/CdS). According to simulations conducted using the SCAPS-1D software, the optimal values for the thickness of the CZTS/CdS layers and the modifier concentration are determined to be 50 nm and 1.5×10^{17} cm^{-3}, respectively [32]. However, the achieved efficiencies of 12.6% $Cu_2ZnSn(S,Se)_4$ (CZTSSe), 11.6% (CZTSe) and 9.4% (CZTS) still fall short when contrasted with the theoretical SQ efficiency of ~30.0% [14, 33, 34].

1.2 Defects in absorbent CZTS layers

Samples without secondary phases and with stoichiometric deviations may have a significant number of intrinsic defects, such as vacancies of Cu, Zn, Sn and S (V_{Cu}, V_{Zn}, V_{Sn} and V_S), interstitials (Cu_i, Zn_i, Sn_i and S_i) and antisite defects involving the substitution of element B with element A (Cu_{Zn}, Zn_{Cu}, Zn_{Sn} and Sn_{Zn}, etc.) [24]. Furthermore, complex defects also referred to as 'clusters', such as ($V_{Zn} + Sn_{Zn}$), ($Sn_{Zn} + Zn_{Sn}$), ($V_{Cu} + Zn_{Cu}$), ($Cu_{Zn} + Zn_{Cu}$), ($Cu_{Sn} + Sn_{Cu}$), ($Zn_{Sn} + 2Zn_{Cu}$) and ($2Cu_{Zn} + Sn_{Sn}$). It emerges because its formation energy is lower than that of individual antisite defects [23]. Moreover, the significant reduction in open-circuit voltages can be attributed to low carrier concentrations and high defect concentrations, the presence of secondary phases and pronounced recombination issues, all of which collectively diminish the performance of the PV device [37]. Fig. 3b illustrates the ionization states of native defects within the forbidden band of CZTS. The summary of potential individual and complex defects in CZTS is presented in Table 4.

2 Substituted or modified CZTS

The quest for thin-film semiconductors with enhanced optical and electrical properties for application in PV cells has prompted researchers to modify kesterite materials (CZTS) by incorporating atoms of different elements into their crystal lattice, deviating from their elemental composition (Cu, Zn, Sn and S) and 2:1:1:4 stoichiometry. An ideal PV material should exhibit a high density of modifying elements, longer carrier lifetimes and minimal recombination losses [38]. On the other hand, a classification can be made between unintentional (intrinsic) and intentional (extrinsic) modifiers, wherein the former entails numerous defects, including vacancies, antisites and interstitials, as well as the formation of complex or cluster defects. Depending on the concentration of elemental impurities in the kesterite, the latter can be further categorized as modifiers and alloying elements. Fig. 3c describes the modifying and alloying elements [35]. Modifiers aim to alter the charge transport, electrical and interface properties of the material while maintaining the crystal structure and preserving the optical properties of the host material.

On the other hand, alloying involves the substitution of an isoelectronic cation to modify the ionic size of the crystal lattice. A description of the modified materials will follow, starting with various metals of interest. These include alkali metals, alkaline earth metals, transition metals and others.

2.1 Alkali metal-modified kesterite materials

These modifying elements increase the concentration of voids, reduce defect points, promote absorber crystal growth and passivate the grain boundaries [39]. Sodium can increase the carrier concentration and enhance the open-circuit voltage (V_{oc}). Similarly, adding potassium as a modifier can result in a preferred positioning regarding the [1 1 2] plane, improving the crystallinity of CZTS thin films and suppressing secondary phases such as ZnS [36]. Fig. 3d depicts the structure of zinc-blende CZTSe (JCPDS no. 70-8930) for samples modified using alkali metals. According to Fig. 3e, each sample of CZTSSe modified using alkali metals exhibits slight changes in diffraction angles compared with the unmodified samples. These changes can be attributed to the increased lattice constants when the materials are modified. The larger lattice constants are caused by the occupation of alkali metal atoms in copper vacancies (V_{Cu}) or its substitution in the CZTSSe atomic positions [18]. Likewise, it was found that the order of achieving the best performance in PV devices when using alkaline modifiers in kesterite materials is as follows: Li > Na > K > Rb > Cs [40]. Moreover, the most favourable outcome was observed when using a lithium-like metal modifier of kesterite materials and it can be attributed to the close ionic radius of Li^+ (0.73 Å) compared with Cu^+ (0.74 Å) and Zn^{2+} (0.74 Å). Despite a reduction in carrier density caused by certain Li atoms taking up positions in V_{Cu}, the materials modified using Li maintain a relatively high carrier density (1.4×10^{15} cm^{-3}) compared with other materials modified using K, Na, Rb and Cs, with studied values of 9.9×10^{14}, 6.8×10^{14}, 5.6×10^{14} and 4.8×10^{14} cm^{-3}, respectively [35, 36]. Table 5 presents various optoelectronic parameters of the CZTSSe absorber material with alkali metals.

Caesium is the only element that compromises the performance of the device and is negatively impacted by its significant incompatibility with CZTSSe in its crystal structure, adversely affecting the roughness of the absorber layer. Additionally, Cs^+ has an ionic radius of 1.81 Å, which is considerably larger than the

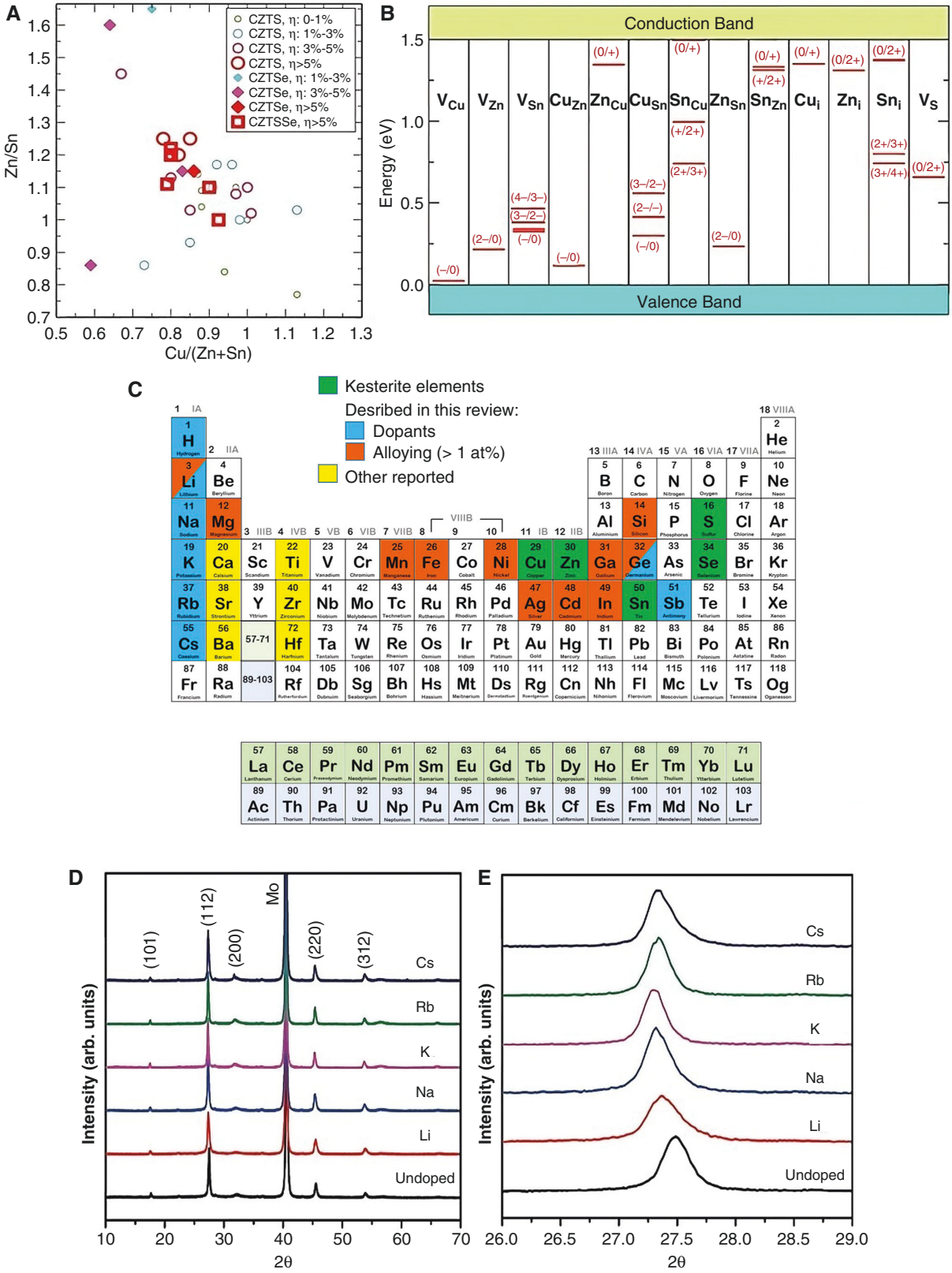

Fig. 3: (a) Element ratios (Cu/Zn + Sn) and (Zn/Sn) for CZTS, CZTSe and CZTSSe, based on solar cells with different efficiency conversion; reproduced from [24] with permission from John Wiley and Sons; (b) ionization levels of intrinsic defects in the band gap of CZTS, where red bars represent the acceptor levels and blue bars represent the donor levels, with initial and final charge states in parentheses; reproduced from [24] with permission from John Wiley and Sons; (c) doping and alloying elements; reproduced from [35] with permission from the author; (d) XRD patterns of CZTSSe thin films modified using alkali metals; reproduced from [36] with permission from John Wiley and Sons; (e) magnification of XRD patterns from 26.0° to 29.0°; reproduced from [36] with permission from John Wiley and Sons.

Table 4: Possible individual and complex defects of the CZTS material [23]

	Details of defects	Ionization levels (donor/acceptor)	Impact on CZTS solar cell performance
Vacancies	V_{Cu}	One, acceptor	◦Ionized from neutral to –1 state and transition level, $\varepsilon(-/0)$ forms shallow state, beneficial for higher solar cell efficiency
	V_{Zn}	Two, acceptor	◦Not favourable, deep levels
	V_{Sn}	Four, acceptor	◦Adversely affect device performance, deep levels
	V_S/V_{Se}	One/one, donor/donor	◦Not favourable, mid-gap states
Antisites	Cu_{Zn}	One, acceptor	◦Deeper than copper vacancy, contribute to the p-type nature of CZTS
	Zn_{Cu}	One, donor	◦Not favourable, shallow level near conduction band
	Cu_{Sn}	Three, acceptor	◦Not favourable, deep and multiple levels
	Sn_{Cu}	Two, donor	◦Not favourable, deep level/mid gas state
	Zn_{Sn}	Two, acceptor	◦Not favourable, deep levels
	Sn_{Zn}	Two, donor	◦Not favourable, mid-gap states
Interstitials	Cu_i	One, donor	◦Not favourable, shallow states near conduction band
	Zn_i	Two, donor	◦Not favourable, mid-gap states
Defect complex (cluster)	Stoichiometric-conserving defect complex $(Cu_{Zn} + Zn_{Cu})$, $(Cu_{Sn} + Sn_{Cu})$, $(Zn_{Sn} + Sn_{Zn})$	$(Cu_{Zn} + Zn_{Cu})$: ~0.2 eV, formation energy; for other two: >0.2 eV	◦$(Cu_{Zn} + Zn_{Cu})$: low impact on optoelectronic properties; other two have significant impact on CZTS and decrease band gap by 0.3 eV
	Non-stoichiometric-conserving defect complex $(V_{Cu} + Zn_{Cu})$, $(V_{Zn} + Sn_{Zn})$, $(Zn_{Sn} + 2Zn_{Cu})$, $(2Cu_{Zn} + Sn_{Sn})$	Formation energy of 0.2–0.6 eV	◦Significant impact and responsible for local variation in chemical potential and stoichiometric inhomogeneity

Table 5: Optoelectronic parameters measured on CZTSSe-modified absorber material with alkaline elements

Modifying element	Material	E_g	V_{oc} (V)	J_{sc} (mA/cm^2)	Fill factor %	Power conversion efficiency %	Source
Unmodified	CZTSSe	1.13	0.513	35.20	69.80	12.60	[14]
Li	CZTSSe	1.11	0.496	35.20	65.80	11.50	[40]
Na	CZTSSe	1.08	0.300	33.90	43.30	4.40	[41]
K	CZTSSe	1.04	0.405	30.90	62.20	7.78	[42]
Rb	CZTSSe	1.08	0.360	30.00	47.50	6.40	[43]
Cs	CZTSSe	–	0.349	22.77	43.71	3.48	[36]

Table 6: Optoelectronic parameters are measured in absorber materials modified using alkaline earth elements

Substituent element	Material	E_g	V_{oc} (V)	J_{sc} (mA/cm^2)	FF (%)	Power conversion efficiency (%)	Method	Source
No substitution	CZTSSe	1.13	0.513	35.20	69.80	12.60	Approximate hydrazine solution/ spin-coating/ chemical bath deposition/ sputtering	[14]
Ca	Cu_2CaSnS_4	1.00	–	–	–	–	Density functional theory	[45]
Mg	Cu_2MgSnS_4	1.45	0.157	16.99	29.20	0.78	Spin-coating/2-methoxyethanol	[49]
Ba	Cu_2BaSnS_4	–	0.551	5.95	48.90	1.60	Co-sputtering	[50]
Ba	$Cu_2BaSn(S,Se)_4$	1.55	0.611	17.40	48.90	5.20	Co-sputtering	[51]
Ba	Cu_2BaSnS_4	2.03	0.933	5.08	42.90	2.03	Co-sputtering	[52]
Sr	Cu_2SrSnS_4	1.93	0.296	1.63	34.00	0.16	Sol–gel/2-methoxyethanol/spin-coating	[53]
Sr	Cu_2SrSnS_4	1.50	0.380	3.80	41.00	0.59	Co-sputtering (Cu, Sr and Sn)	[54]

Cu^+ ionic radius of 0.74 Å, leading to atom substitution within the CZTSSe material [36]. Furthermore, each alkaline element requires optimal concentrations to promote favourable morphology and achieve high performance in PV devices [40].

2.2 Alkaline earth metal-modified kesterite materials

The most commonly used elements in this group for modifying kesterite materials are magnesium (Mg), strontium (Sr)

and barium (Ba), with calcium (Ca) used in smaller proportions. Alkaline earth elements possess low toxicity, can form compounds with various metals, are abundant, are environmentally friendly and exhibit high chemical reactivity [44]. However, calcium encounters challenges when incorporated into the crystal lattice of kesterite. Moreover, it can create secondary phases when utilized in higher proportions as a modifier. Furthermore, the thermodynamic instability of CZTS with high calcium (Ca) contents can be associated with the combined effects of large ions and high oxidation states. Therefore, modifying kesterite materials with an important bulk of Ca within the crystal lattice may not be feasible, as demonstrated by the compound $Cu_2Ca_{0.5}Zn_{0.5}SnS_4$, which could decompose into CZTS, Cu_2SnS_3 and CaS [45]. Some studies use the density functional theory (DFT) to predict the behaviour of modified kesterite materials. One example is the Vienna *ab initio* simulation package (VASP) software. In this approach, modifying cations such as Na^+ and Ca^{2+} are considered isovalent with Cu^+ and Zn^{2+} and located in antisite positions.

Similarly, incorporating calcium (Ca) into the kesterite structure results in Ca_{Cu} and Ca_{Zn} antisite defects, with corresponding formation energies of 2.5 and 2.41 eV. These defects hinder the introduction of Ca into the crystal lattice [45]. In the same way, the VASP software was employed as a simulation tool to replace the Zn atom with Be, Mg, Ca, Fe and Ni atoms at the X position of the kesterite (CXTS). This was done to evaluate, reduce and control cation disorders in CZTS, as it is considered the most significant challenge due to the low formation energies of the antisite pairs ($Cu_{Zn} + Zn_{Cu}^{+}$) [46]. Similarly, to control cation disorder, Zn^{2+} (having an ionic radius of 0.74 Å) was replaced by Ba^{2+} (having an ionic radius of 1.56 Å) and Sr^{2+} (having an ionic radius of 1.40 Å) in the $Cu_2BaSn(S,Se)_4$ and $Cu_2SrSn(S,Se)_4$ systems. Consequently, a high formation energy for Cu–Ba/Sr and Sn–Ba/Sr antisite defects was obtained. This can be attributed to the significant mismatch in ionic radii between Ba_2+/Sr_2 + and Cu_{2+}/Sn_{4+} cations and the significant difference in the electronic properties of Ba and Sr in contrast to Cu and Sn [47, 48]. Table 6 presents the optoelectronic properties of alkaline earth elements and the synthesis methods employed. It can be observed that group II metals exhibit low energy-conversion efficiencies, which is attributed to their role as Zn substitutes rather than extrinsic modifiers of the CZTS absorber material.

Furthermore, there are significant mismatches in ionic radii between Zn and Ca, Ba and Sr, as shown in Table 7. These mismatches result in antisite defects and variations in optoelectronic properties. Similarly, the fill factor (FF) is considerably

Table 7: The ionic radius of constituent metals of kesterite is based on M^{I}, M^{II}, M^{III} and M^{IV} chalcogenides [55]

M^{I} ionic radii (Å)	Cu^+ 0.74		Ag^+ 1.14		Li^+ 0.73						
M^{II} ionic radii (Å)	Zn^{2+} 0.74	Cd^{2+} 0.92	Mg^{2+} 0.71	Ca^{2+} 1.14	Sr^{2+} 1.32	Ba^{2+} 1.49	Mn^{2+} 0.80	Fe^{2+} 0.77	Co^{2+} 0.72	Ni^{2+} 0.69	Pb^{2+} 1.12
M^{III} ionic radii (Å)	In^{3+} 0.76	Ga^{3+} 0.61									
M^{IV} ionic radii (Å)	Sn^{4+} 0.69	Ge^{4+} 0.53	Si^{4+} 0.40								

Table 8: Optoelectronic parameters measured on magnesium-substituted absorber materials, CMTS and CMTSSe

Substituent element	Material	Type	n (cm^{-3})	μ (cm^2 V^{-1} s^{-1})	E_g	V_{oc} (V)	J_{sc} (mA cm^{-2})	FF (%)	Power conversion efficiency (%)	Grain size (μm)	Method	Year	Source
No substitution (record)	CZTSSe	p	–	–	1.13	0.513	35.20	69.80	12.60	2.000	Approximate hydrazine solution/spin-coating/ CBD/sputtering	2013	[14]
Mg	Cu_2MgSnS_4	–			1.63	–	–	–	–	0.010	Hot injection	2014	[58]
Mg	$Cu_2MgSnSe_4$	p	3.20×10^{18}	51.70	1.70	–	–	–	–	–	Solid-state reaction	2015	[59]
Mg	Cu_2MgSnS_4	p	5.30×10^{18}	8.34	1.76					–	Dual-source ultrasonic co-spray	2016	[60]
Mg	Cu_2MgSnS_4	–	–	–	1.48	–	–	–	–	–	Density functional theory	2017	[46]
No substitution (record)	CZTS	–	–	–	1.50	0.731	21.74	69.27	11.01	–	Hot treatment	2018	[56]
Mg	Cu_2MgSnS_4	p	–	–	1.45	0.160	16.99	29.20	0.78	0.400	Spin-coating/2-methoxyethanol	2019	[49]
Mg	Cu_2MgSnS_4	–	–	–	1.56	–	–	–	–	0.050	Spray pyrolysis	2020	[61]
Mg	Cu_2MgSnS_4	p	–	–	1.95	–	–	–	5.11	0.004	Sol–gel/spin-coating	2020	[57]
Mg	$Cu_2MgSnSe_4$	p	–	–	1.40	–	–	–	–	–	Graphitized quartz ampules sealed off under vacuum/ annealed to 600–750°C	2021	[62]
Mg	Cu_2MgSnS_4	–	–	–	1.50	–	–	–	–	0.020	Spray pyrolysis	2022	[63]

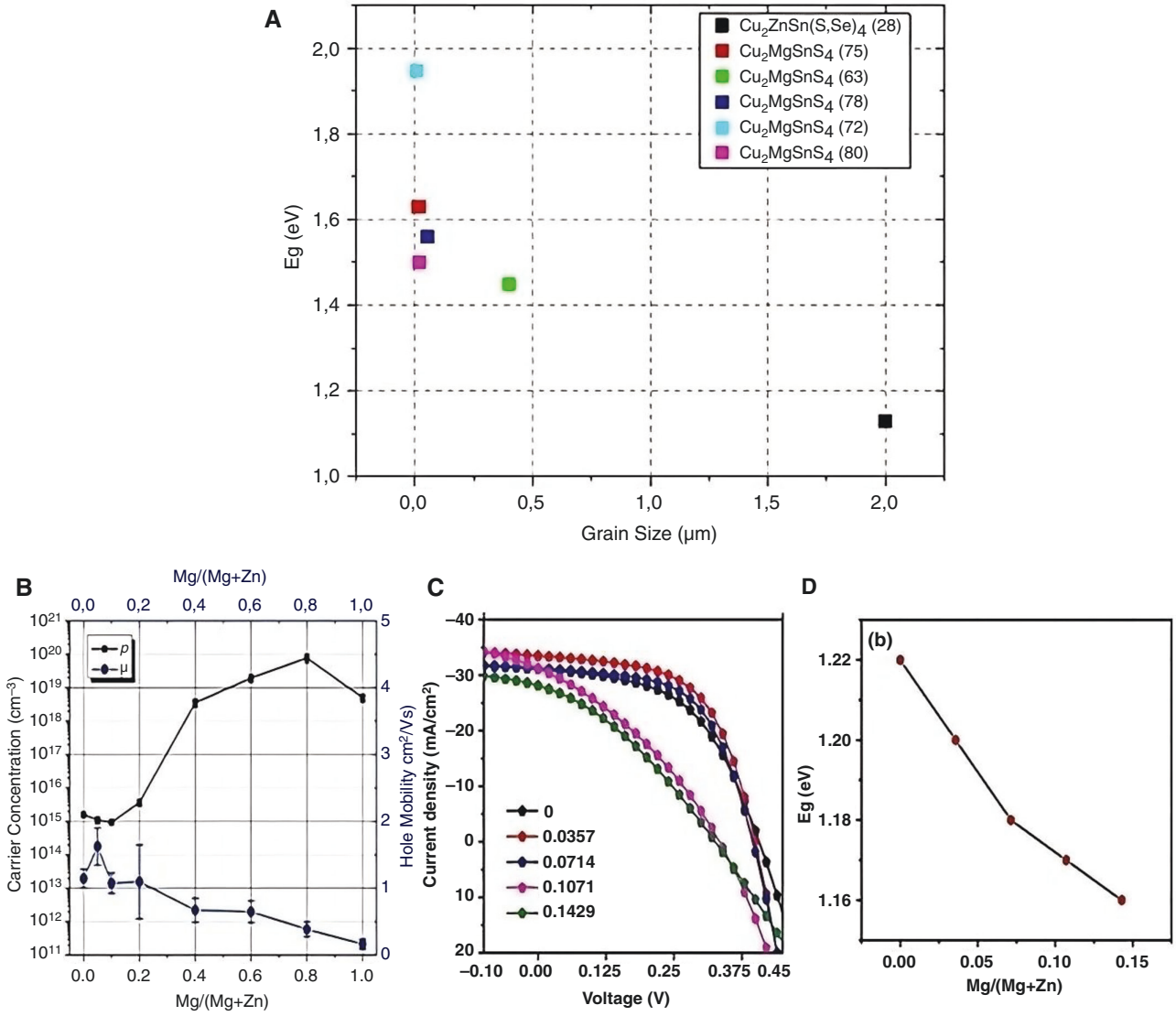

Fig. 4: (a) Influence of grain size with respect to band gap, as reported by different authors; optoelectronic results of Mg incorporation in the materials; (b) $Cu_2Mg_xZn_{1-x}SnS_4$ reproduced from [20] with permission from the American Chemical Society; (c) and (d) $Cu_2Mg_xZn_{1-x}Sn(S,Se)_4$ reproduced from [67] with permission from the American Chemical Society.

lower than the unsubstituted material, and some open-circuit voltages (V_{oc}) do not align with the reported efficiencies. Additionally, mentioning that the kesterite band gap should typically fall within 1.0–1.5 eV [9] is essential. However, most reported values are either at the limit or outside the predetermined range, indicating the lack of tunability in certain materials. Consequently, this results in a significant decrease in the performance of PV devices.

Concerning Mg^{2+}, the ionic radius of this cation is very similar to that of Zn^{2+} (as shown in Table 7), which facilitates its substitution and the formation of the Cu_2MgSnS_4 (CMTS) material. Furthermore, it crystallizes in a single zinc-blende structure and XRD analysis confirms the lack of signals associated with the kesterite structure and secondary phases [49]. In the same way, its efficiency of 0.78% is low compared with that of unsubstituted kesterite (12.6%). However, there was an improvement in its optoelectronic properties, including the open-circuit voltage (V_{oc}), short circuit current (J_{sc}) and FF, when subjected to temperatures of 530°C. This temperature treatment enhanced crystallinity and improved the CMTS/CdS interface.

2.3 Zinc substituted by magnesium in kesterite materials

One of the primary motivations for substituting Mg in kesterite (CZTS) as an alternative to Zn is its remarkably similar ionic radius [27]. Similarly, Table 7 presents various ionic radii of the constituent metals in kesterite. Additionally, Mg^{2+} can be substituted by Zn^{2+} due to its abundance in Earth's crust, non-toxicity and cost-effectiveness.

The efficiencies achieved for CZTS and CZTSSe kesterite materials are 11.01% and 12.6%, respectively [14, 56]. However, the presence of antisite defects (Cu_{Zn}, Zn_{Cu}) impairs the efficiency of the PV cells. Moreover, Zn could be substituted by closely related transition elements such as Ni, Co, Fe, Mn and Cr or with group IIA elements such as Be, Ca, Mg, Sr and Ba, as well as group IIB elements such as Cd and Hg, to remove these defects and enhance the performance of the PV cells. Nevertheless, despite the superior stability achieved by using Be, Cd and Hg, these elements are being replaced due to their high toxicity [57].

On the other hand, among the most viable candidates to replace Zn, Mg stands out. Mg has the same valence state as Zn and

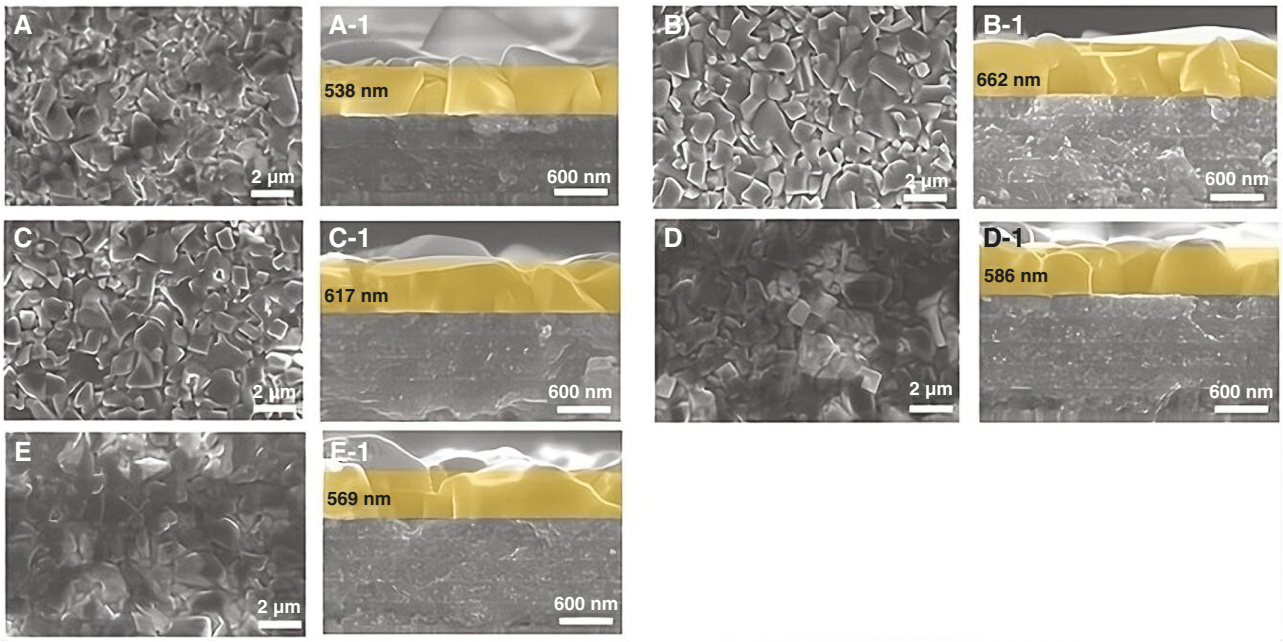

Fig. 5: Morphology and cross section of the material $Cu_2Mg_xZn_{1-x}Sn(S,Se)_4$, obtained from SEM and referenced with stoichiometric values of x = 0.0 (a and a-1), 0.0357(b and b-1), 0.0714 (c and c-1), 0.1071 (d and d-1) and 0.1429 (e and e-1), respectively. Reproduced from [67] with permission from the American Chemical Society.

a similar ionic radius, with Mg^{2+} corresponding to 0.71 Å and Zn^{2+} corresponding to 0.74 Å, respectively [27, 55]. Furthermore, Mg is thermodynamically stable and effectively reduces antisite defects due to its larger atomic size. Table 8 presents the optoelectronic properties of Mg-substituted Zn cations in kesterite materials, such as the carrier concentration shown as *n*, mobility as μ, band gap as E_g, open-circuit voltage as V_{oc}, short-circuit current as J_{sc} and fill factor as *FF* [64]. Additionally, thin-film absorber materials such as CMTS and $Cu_2MgSn(S,Se)_4$ (CMTSSe) and unsubstituted materials CZTS and CZTSSe serve as benchmarks. According to Table 8, the availability of optoelectronic reports conducted by various authors is limited or absent in the literature. This lack of literature can be attributed to the scarcity of studies on the substituted thin-film absorber materials Cu_2MgSnS_4 and $Cu_2MgSnSe_4$.

Additionally, it is notable that various synthesis methods have been employed, except for hydrothermal synthesis, which presents an excellent opportunity for research and diffusion. As for band-gap tuning, it should fall within the range of 1.0–1.5 eV. However, the band gap of the material varies from 1.39 to 1.94 eV, sometimes exceeding the optimal range [9]. This can be attributed to the inverse relationship between the particle size and the band gap of the material, as the band gap decreases with increasing particle size [65]. In the first row of Table 8, the recorded data indicate a grain size of 2 µm and a band gap of 1.13 eV for the CZTSSe material [14]. However, the materials mentioned in Table 8 and depicted in Fig. 4a have relatively small particle sizes ranging from 0.004 to 0.4 µm, which leads to an increase in the band-gap values (1.39–1.95 eV) and adversely affects the efficiency of the reported PV cells.

2.4 Magnesium as a modifier in kesterite materials

Cation disorders in kesterite (CZTS) could be the underlying origin of the low performance of PV devices and the presence of antisite defects (Cu_{Zn}, Zn_{Cu}) that function as recombination centres. Likewise, secondary phases (Cu_2SnS_3, Cu_2S, SnS_2 and ZnS) contribute to low open-circuit voltages and high resistances, making their identification challenging [66]. Fortunately, the issue of defects caused by cation disorders can be resolved by substituting Cu or Zn with other metallic elements that can prevent such formation [27]. Moreover, adding Mg as a modifier can result in the formation of the $Cu_2Mg_xZn_{1-x}Sn(S,Se)_4$ (CMZTSSe) phase, adjustment of the band gap, improvement in layer thickness and grain size, and increased carrier concentration in the absorber layer, thereby enhancing device performance [67]. However, regardless of the concentration, all Mg-modified CZTSe materials behave as n-type semiconductors, indicating that Mg functions as a donor [68]. Nevertheless, another study reported the absence of n-type behaviour in $Cu_2Zn_{1-x}Mg_xSnS_4$ (CZMTS) thin films, even with the complete substitution of Zn^{2+} by Mg^{2+} [69]. On the other hand, it has been reported that, when Zn is substituted with elements from group IIA in compounds of the type I_2–II–IV–VI_4, instability is observed [70]. Nevertheless, the incorporation of magnesium as a modifier at low concentrations appears to enhance both the stability and the optoelectronic properties of these compounds [71]. Fig. 4b–d presents various studies on the incorporation of Mg as a modifier in low concentrations. In Fig. 4b, the decrease in mobility is depicted as the Mg concentration increases in the $Cu_2Mg_xZn_{1-x}SnS_4$ material with the ratio of Mg/(Mg + Zn) [20]. Furthermore, the material achieves maximum mobility values at low Mg concentrations (x = 0.05). However, when the Mg concentration exceeds $x \geq 0.05$, there is an increase in the carrier concentration but a decrease in the mobility. Fig. 4c and d also demonstrates that the highest current density is attained when the Mg composition ratio is 0.0357. Simultaneously, with the rising Mg concentration, the band gap experiences a decrease in the $Cu_2Mg_xZn_{1-x}Sn(S,Se)_4$ material, represented by the ratio of Mg/(Mg + Zn) [67].

Recently, a study investigated the impact of Mg concentration as a modifier, with stoichiometric values of x = 0.0, 0.0357, 0.0714, 0.107 and 0.1429, respectively [67]. Fig. 5a–e and a-1–e-1 display the morphology and cross section of the $Cu_2Mg_xZn_{1-x}Sn(S,Se)_4$ material,

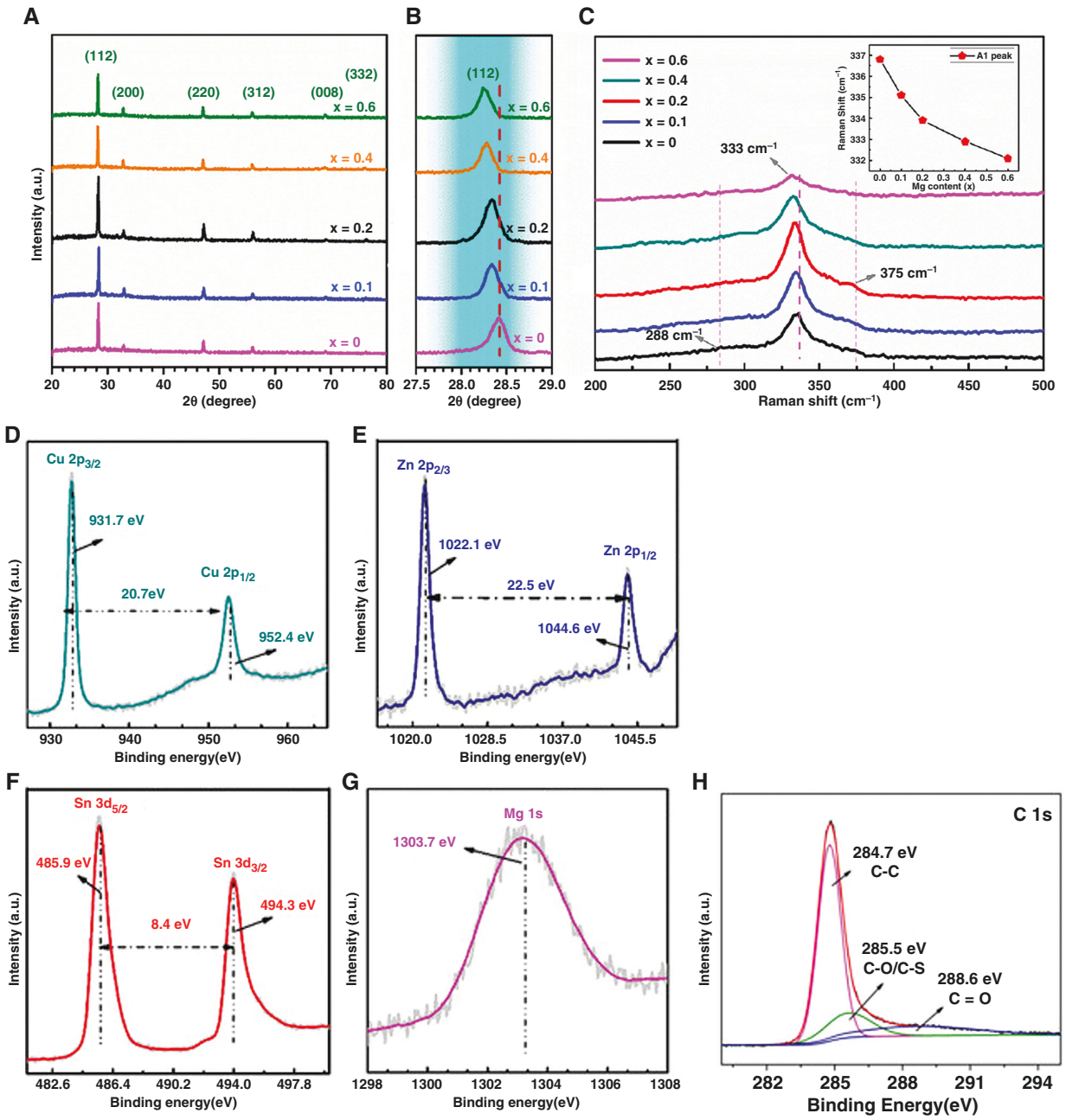

Fig. 6: Material $Cu_2Mg_xZn_{1-x}SnS_4$. (a) X-ray diffraction of thin film ($0 \le x \le 0.6$); (b) diffraction plane magnification [1 1 2]; (c) Raman shift for material; X-ray photoelectron spectroscopy (XPS) of the $Cu_2Mg_xZn_{1-x}SnS_4$ (CMZTS) absorber layer: (d) Cu; (e) Zn; (f) Sn; (g) Mg; (h) high-resolution scanning by using X-ray photoelectron spectroscopy of carbon (C 1s) X-rays in CZTS and CZMTS absorber layers. (a)–(g) reprinted with permission from [72]; (h) reproduced from [73] with permission from John Wiley and Sons.

as observed through using scanning electron microscopy (SEM). In conclusion, when $x = 0.0357$, the material exhibits more defined, smooth, homogeneous and crack-free grain sizes. Furthermore, the cross section of the $Cu_2Mg_{0.0357}Zn_{0.9643}Sn(S,Se)_4$ absorber material demonstrates the highest thickness (662 nm) compared with the other thin films and the unmodified material (538 nm).

On the other hand, XRD and Raman spectroscopy are instrumental techniques commonly employed to assess the crystalline quality and identify the existence of secondary phases. These techniques have been utilized to evaluate thin-film materials modified using $Cu_2Mg_xZn_{1-x}SnS_4$ ($0 \le x \le 0.6$). The strongest diffraction signals were observed at 2θ angles of 28.53°, 32.99°, 47.33° and 56.17°, corresponding to the diffraction planes of kesterite [1 1 2], [2 0 0], [2 2 0] and [3 1 2] (JCPDS no. 26-0575), respectively, as depicted in Fig. 6a and b [72]. It is worth mentioning that no secondary phases were detected, indicating that the modification using Mg does not impact the kesterite crystal structure, as illustrated in Fig. 6c. However, as the Mg content increased, a shift of 0.08° was observed in the diffraction plane [1 1 2], increasing the lattice constants of the $Cu_2Mg_xZn_{1-x}SnS_4$ thin-film material. Simultaneously, the Raman signals were associated with the A1, A2 and E vibrational modes of the sulphur atom in the kesterite, respectively. Additionally, the shift of the A1 vibrational mode from 333.69 to 332.13 cm^{-1} could be associated with the lattice expansion resulting from the substitution of Zn^{2+} (0.74 Å) by Mg^{2+} (0.71 Å) [27].

Table 9: Optoelectronic parameters measured in magnesium-modified absorber materials

Modifier element	Material	Type	n (cm^{-3})	μ ($cm^2 V^{-1} s^{-1}$)	E_g	V_{oc} (V)	J_{sc} (mA cm^{-2})	FF (%)	PCE (%)	Grain size (μm)	Method	Year	Source
Unmodified (record)	CZTSSe	p	–	–	1.13	0.5134	35.2	69.8	12.6	2.00	Approximate hydrazine solution/spin coating/CBD/ sputtering	2013	[14]
Mg	$Cu_{1.9}Mg_{0.1}ZnSnSe_4$	n	1.03×10^{18}	120.0	–	–	–	–	–	–	Reactive sintering	2014	[68]
Unmodified (record)	CZTS	–	–	–	1.50	0.730	21.74	69.30	11.01	–	Hot treatment	2018	[56]
Mg	$Cu_2Zn_{0.5}Mg_{0.5}SnS_4$	p	1.95×10^{18}	13.2	1.42	–	–	–	–	–	Pulsed laser deposition	2018	[69]
Mg	$Cu_2Zn_{0.96}Mg_{0.04}Sn(S,Se)_4$	–	–	–	1.01	0.420	37.20	46.50	7.20	–	Approximate solution/selenium atmospheric annealing	2018	[70]
Mg	$Cu_2Mg_{0.05}Zn_{0.95}SnS_4$	P	–	–	1.54	0.670	17.19	59.40	6.73	–	Spray pyrolysis/ sulphuration	2019	[20]
Mg	$Cu_2Mg_{0.2}Zn_{0.8}SnS_4$	P	3.30×10^{18}	0.1	1.40	–	–	–	–	1.50	Sol–gel/spin-coating/ annealing 580°C	2019	[72]
Mg	$Cu_2Mg_{0.2}Zn_{0.8}Sn(S,Se)_4$	P	6.50×10^{18}	0.3	1.02	–	–	–	–	2.50	Sol–gel/ spin-coating/ selenization	2019	[76]
Mg	$Cu_2Mg_{0.0357}Zn_{0.9643}Sn(S,Se)_4$	–	8.80×10^{17}	–	1.20	0.400	33.45	57.93	7.80	–	Spin-coating/ chemical bath deposition	2020	[67]
Mg	$Cu_2Mg_{0.05}Zn_{0.95}SnS_4$	p	2.40×10^{16}	6.3	1.54	0.700	15.32	39.20	4.10	1.00	Solution DMF/ spin-coating/ sulphuration	2021	[27]

The X-ray photoelectron spectroscopy (XPS) results are presented in Fig. 6d–h, which illustrates the oxidation states of the modified kesterite $Cu_2Mg_{0.05}Zn_{0.95}SnS_4$. These figures correspond to the Cu 2p, Zn 2p, Sn 3d and Mg 1s spectra [27, 72]. Fig. 6d–f depicts the spectra Cu $2p_{1/2}$ and Cu $2p_{3/2}$, Zn $2p_{1/2}$ and Zn $2p_{3/2}$, Sn $3d_{3/2}$ and Sn $3d_{5/2}$, showing double signals. These signals coincide with the values previously reported [74, 75]. In addition, it was found that the binding energy of Mg 1s shown in Fig. 6g (1303.7 eV) is equivalent to that in a previous report (1303.6 eV) [76] and that the easing of the solution method allowed the successful incorporation of Mg, without generating changes in the valence of the CZMTS material. On the other hand, the differences in binding energies (ΔE) corresponding to the double signals are consistent with the valence states Cu^{+1}, Mg^{+2}, Zn^{+2} and Sn^{+4}, respectively. Another essential feature that has been reported is the detection of carbon impurities in CZTS and $Cu_2Mg_xZn_{1-x}SnS_4$ (CMZTS) PV materials. These impurities result from the decomposition of organic solvents during the synthesis process, and it cannot be identified by XRD but can be disclosed through XPS. Previous reports have uncovered carbon traces using the high-resolution XPS technique. In the case of the CZTS adsorbent material, the atomic percentage of carbon impurities was determined to be 6.43%. Following the modification with Mg, the CMZTS absorber material showed an atomic ratio of carbon impurities of 5.46% [27]. Moreover, the C–O/C–N spectrum disappeared and the area of the C=O spectrum decreased, indicating a transition towards C–C (284.7 eV). Fig. 6h illustrates the C 1s spectrum, which can be separated into three distinct spectra through the deconvolution process: unoxidized C–C (284.7 eV), C–O/C–S (285.5 eV) and C=O (288.6 eV) [27, 73]. In conclusion, the decrease in carbon impurity levels could lead to a slight increase in the efficiency of the CMZTS cell.

It should be noted that the reduction in carbon residues (3 % at.) during the synthesis of kesterite materials had already been reported [77]. This reduction is attributed to the implementation of the air annealing process. In addition, the decomposition of metal–thiourea–oxygen complexes under an oxygen atmosphere proves advantageous in reducing the carbon or nitrogen contents in thin films. This process involves the breaking and oxidation of C–H and C–O bonds in organic solvents [78]. Nevertheless, modifying the CZTS material using cations such as Na^+ is key to reducing carbon impurities. This modification significantly decreases from 5.25% (unmodified CZTS) to 1.13%, respectively.

On the other hand, Table 9 summarizes some optoelectronic parameters reported by different bibliographic references for Mg-modified kesterite materials, except citations [14, 56], which correspond to CZTSSe and CZTS kesterite materials, respectively, placed as reference materials with current records. Fig. 7a–d shows the trend of materials V and VI, which increase the open-circuit voltage (V_{oc}) and band gap while decreasing the short-circuit density (J_{sc}) and power-conversion efficiency (PCE) when the concentration of Mg is equal to $x = 0.05$. However, when x takes values from 0.0357 to 0.04 for materials III and IV, V_{oc} and the band gap decreased, while J_{sc} and the PCE increased. The band gap and PCE improvement in these semiconductors is due to the synthesis method used and the use of selenium

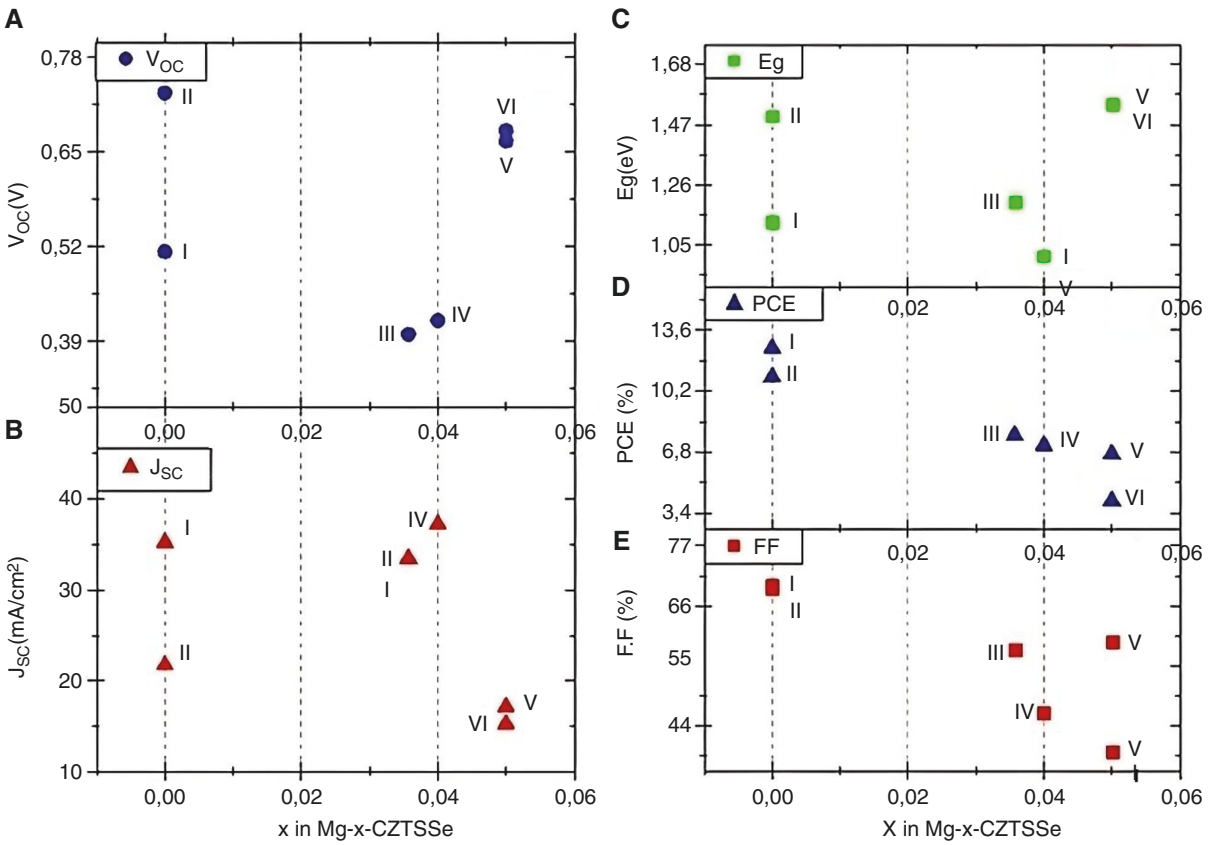

Fig. 7: Comparative analysis of optoelectronic parameters for modified and unmodified materials, shown in Table 9: (I) CZTSSe; (II) CZTS; (III) $Cu_2Mg_{0.0357}Zn_{0.9643}Sn(S,Se)_4$; (IV) $Cu_2Zn_{0.96}Mg_{0.04}Sn(S,Se)_4$; (V) $Cu_2Mg_{0.05}Zn_{0.95}SnS_4$; (VI) $Cu_2Mg_{0.05}Zn_{0.95}SnS_4$

compared with materials that include sulphur. Similarly, the advantages of selenium are tuning the band gap, better efficiency and power output.

In Fig. 7e, materials III–VI exhibit FF values ranging from 39.4% to 59.3%, which are significantly lower than those of unmodified reference materials I (CZTSSe) and II (CZTS), at 69.8% and 69.2%, respectively. Furthermore, a comparison between materials I and II reveals that the former, incorporating selenium, exhibits superior band gap and PCE results. However, selenium is considered a harmful material used in thin-film PV cells. In contrast, the latter material uses sulphur in the composition, which is environmentally friendly, abundant and cheap. Likewise, it shows higher open-circuit voltage (V_{oc}) and low short-circuit density (J_{sc}), identical FF, regarding the Fig. 7A-I material $Cu_2ZnSn(S,Se)_4$ (CZTSSe) and near values of PCE, at 12.6% and 11.0%, respectively. In conclusion, to reduce the band gap and maintain the best results in PCE, the optimum range of the Mg concentration for modified material CMZTS must be 0.03–0.04. However, this concentration of Mg ostensibly reduces the open-circuit voltage (V_{oc}) and increases the short-circuit density (J_{sc}). On the other hand, sulphur is an element that can be a substituent for selenium due to sustainability and is considered free of critical raw materials.

Table 9 also shows that the materials that include selenium in their structure have lower band-gap values of between 1.01 and 1.20 eV, while those with sulphur present higher band-gap values of between 1.35 and 1.54 eV. The consequence of having high band-gap values is reflected in the decrease in the grain size, as well as the FF and efficiency, limiting the performance of the PV cell and leading to a deficit of open-circuit voltages. Likewise, the efficiencies achieved with the selenium-containing Mg-modified materials are higher (7.20–7.76%) compared with sulphur-containing materials (4.10–6.73%), which is associated with the narrowing of the band gap in CZTSSe thin films when the selenium concentration is increased. Additionally, an increase in the FF and open-circuit voltage (V_{oc}), as well as a decrease in the short-circuit density (J_{sc}), is favoured. Similarly, the presence of selenium contributes to tuning the band gap to between 1.0 and 1.5 eV, facilitates matching with the solar spectrum, improves efficiency and current output, alters the concentration carriers (hole density) and maintains the p-type nature of these semiconductors. It was also found that selenium-containing materials exhibit the highest value of concentration carrier (6.47×10^{18} cm^{-3}) compared with sulphur-containing materials (3.29×10^{18} cm^{-3}) [79].

In conclusion, the materials obtained from the modification using Mg present limited information or have not been studied in depth due to their low efficiencies. Likewise, the methods used for synthesizing CMZTS and CMZTSSe materials do not include the hydrothermal method, which could be a viable alternative for achieving low cost. Besides, these materials are environmentally friendly and can improve the durability, efficiency and crystalline distribution of PV cells.

Moreover, using selenium in Mg-modified kesterite materials enhances the efficiency of PV cells. However, trace selenium is essential for human health but is harmful at high concentrations (400 µg/day). Despite patented selenium purification and recovery processes since 1946, CZTSSe recycling methods have not been applied compared with $Cu(In_x,Ga_{1-x})Se_2$ (CIGS) , which have [80].

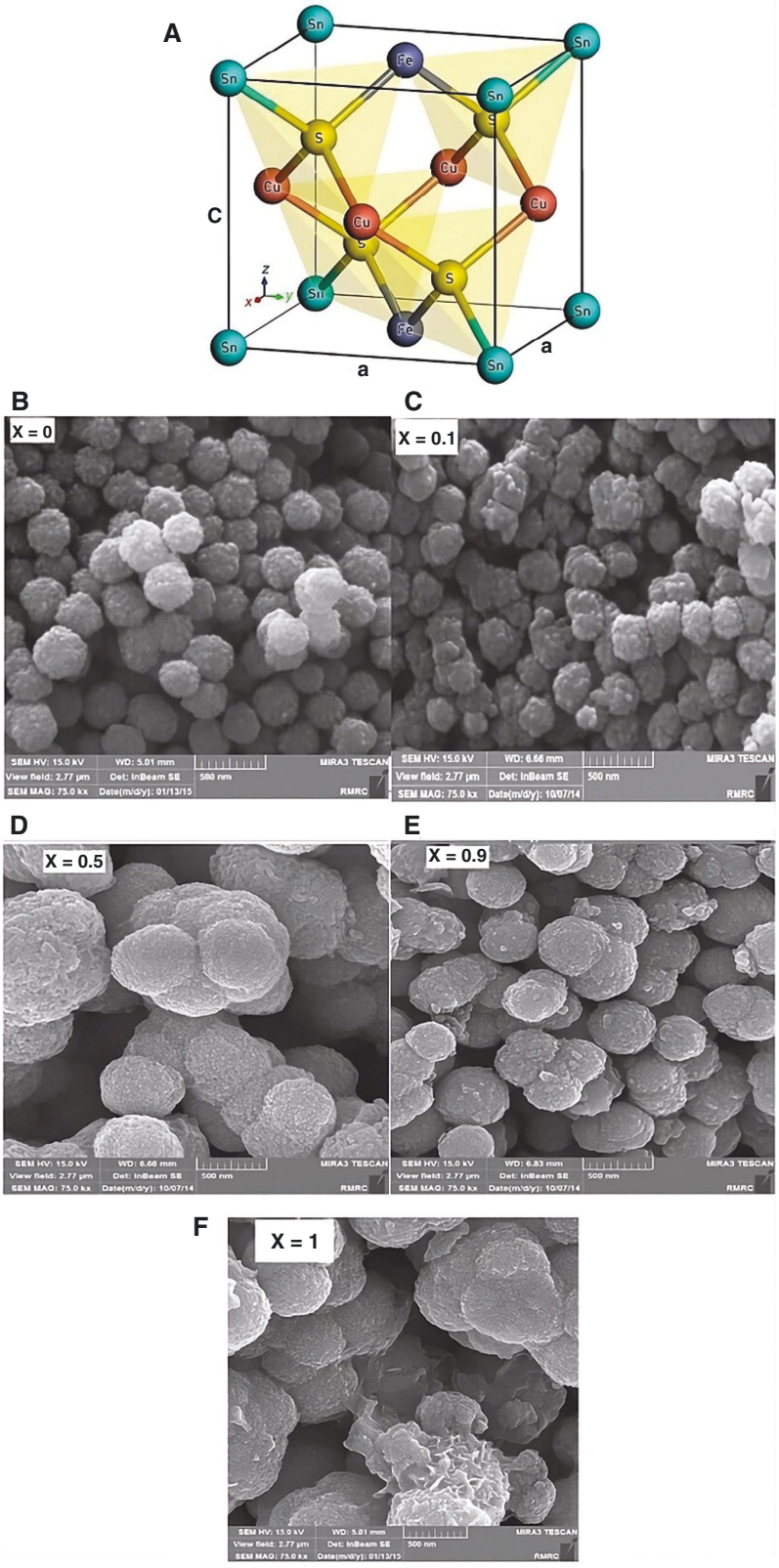

Fig. 8: (a) Crystalline structure of Cu_2FeSnS_4 material (quaternary compound) [88]. Morphological FE-SEM images of CZFTS ($0 \le x \le 1$): (b) $CZ_{1.0}F_{0.0}TS$, (c) $CZ_{0.9}F_{0.1}TS$, (d) $CZ_{0.5}F_{0.5}TS$, (e) $CZ_{0.1}F_{0.9}TS$ and (f) CFTS; reproduced from [84] with permission from IOP Publishing, Ltd.

2.5 Zinc substituted by iron in kesterite materials

According to a previous report, compounds with the structure Cu_2–II–Sn–S_4 (II = Fe, Co and Ni) were obtained by substituting zinc atoms with iron, cobalt or nickel atoms. These compounds exhibit band-gap values of between 1.57 and 1.87 eV. These semiconductor materials can also originate from the diamond-type structure or group IV semiconductors (tetrahedral coordination),

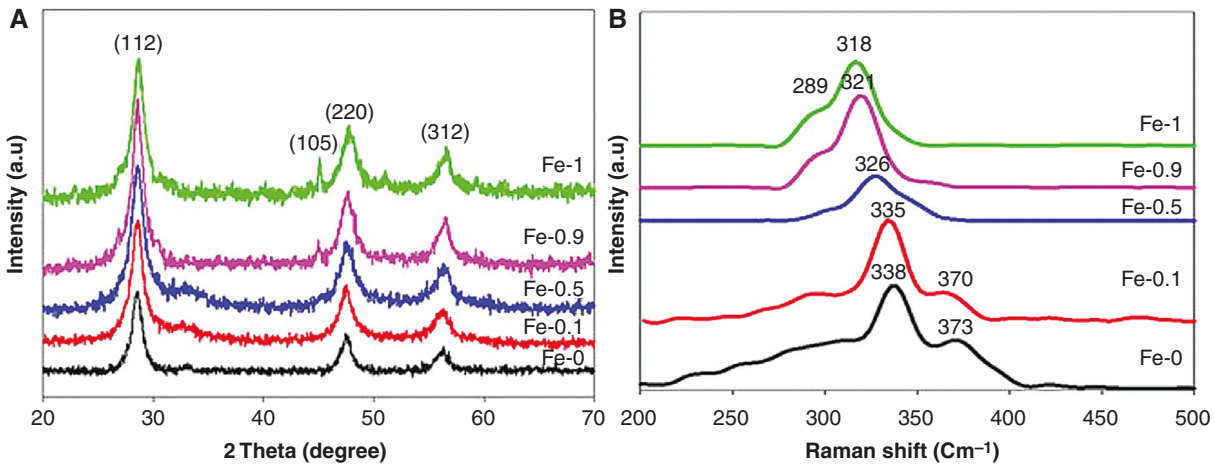

Fig. 9: (a) XRD patterns from the $CZ_{1-x}F_xTS$ ($0 \le x \le 1$) thin films; (b) Raman spectra measured from the $CZ_{1-x}F_xTS$ ($0 \le x \le 1$) alloys, showing the main contributions in the 200–400 cm^{-1} spectral region; reproduced from [84] with permission from IOP Publishing, Ltd.

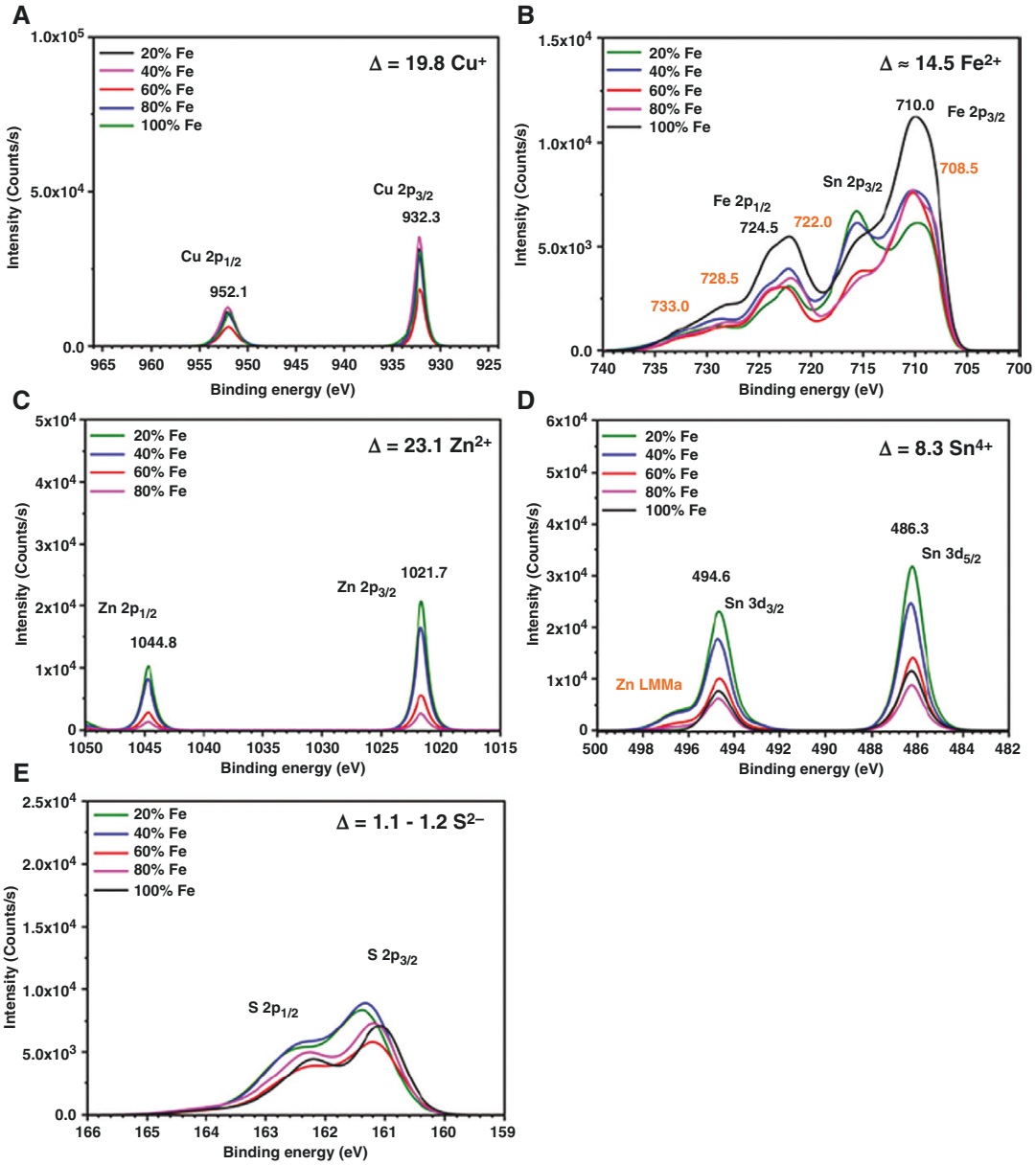

Fig. 10: XPS spectrum of $CZ_{1-x}F_xTS$ ($0 \le x \le 1$) high-resolution spectra to resolve: (a) Cu2p; (b) Zn2p; (c) Fe2p; (d) Sn3d and (e) S2p spectral lines [89]

Table 10: Optoelectronic parameters measured on iron thin-film absorber materials

Substituent element	Material	Type	n (cm^{-3})	μ ($cm^2\ V^{-1}\ s^{-1}$)	E_g	V_{oc} (V)	J_{sc} ($mA\ cm^{-2}$)	FF (%)	PCE (%)	Grain size (μm)	Method	Year	Source
Fe	$Cu_2Zn_{0.75}Fe_{0.25}SnS_4$	–	–	–	1.58	–	–	–	–	0.600	Pulsed laser deposition	2014	[86]
Fe	Cu_2FeSnS_4	–	–	–	1.20	–	–	–	–	0.200	Pulsed laser deposition	2014	[93]
Fe	Cu_2FeSnS_4	–	–	–	1.42	0.110	2.50	26.3	0.07	–	Spraying/ sulphurization	2015	[94]
Fe	Cu_2FeSnS_4	–	–	–	1.87	–	–	–	–	–	Sol–gel/ spin-coating	2016	[95]
Fe	$Cu_2Zn_{0.75}Fe_{0.75}SnS_4$	p	–	–	1.56	–	–	–	–	–	Direct fusion	2017	[96]
Fe	$Cu_2FeSnSe_4$	p	–	–	1.50	0.610	9.30	52.00	2.95	–	Successive ionic layer adsorption and reaction	2017	[90]
Fe	Cu_2FeSnS_4	p	3.30×10^{17}	4.5	–	0.705	17.37	57.00	7.36	0.012	Thermal decomposition	2017	[97]
Fe	$Cu_2FeSnSe_4$	–	–	–	1.67	–	–	–	–	0.006	Wet chemical heating up	2018	[87]
Fe	$Cu_2Zn_{0.25}Fe_{0.75}SnS_4$	–	–	–	1.32	–	–	–	–	0.007	Solvothermal	2018	[98]
Fe	Cu_2FeSnS_4	–	1.27×10^{16}	10.60×10^2	1.05	–	–	–	–	0.041	Spray pyrolysis	2018	[99]
Fe	Cu_2FeSnS_4	–	0.74×10^{17}	1.86×10^2	1.46	–	–	–	–	0.045	Spray pyrolysis	2020	[100]
Fe	Cu_2FeSnS_4	–	–	–	1.19	–	–	–	–	–	Chemical bath deposition	2020	[101]
Fe	$Cu_2Zn_{0.75}Fe_{0.75}SnS_4$	–	–	–	1.38	–	–	–	–	–	Sol–gel	2020	[89]

as depicted in Fig. 8a. Furthermore, group II elements are diamagnetic ions (e.g. II = Zn^{+2}; Cd^{+2}; Hg^{+2}) and can be substituted by paramagnetic ions (e.g. Cr^{+2}; Mn^{+2}; Fe^{+2}; Co^{+2}; Ni^{+2}) to form magnetic semiconductor compounds [81]. A clear example can be found in the synthesis of Cu_2FeSnS_4 (CFTS) and $Cu_2(Mn_{1-x}Fe_x)SnS_4$ ($x = 1, 0.8, 0.6, 0.4, 0.2, 0$) thin-film materials obtained by using the hydrothermal method. However, no optoelectronic parameters evaluated are reported. The first was obtained by maintaining the reaction temperature at between 230°C and 250°C, at constant pressure for 24–36 h and using $CuCl_2$, NH_2CSNH_2, $FeSO_4$ and $SnCl_2$ as precursors. The second one handled temperatures of 160–190°C, at constant pressure and time intervals of 1–14 days, using as precursors water–ethylene glycol (1:7), polyvinylpyrrolidone (PVP) as the binder, $CuCl_2.2H_2O$, $SnCl_4.5H_2O$, $FeCl_2.4H_2O$, $MnCl_2.4H_2O$ and NH_2CSNH_2, respectively [82, 83]. A previous report demonstrated that the solvothermal method can be used to prepare $Cu_2(Zn_{1-x}Fe_x)SnS_4$ (CZFTS) thin films. The introduction of iron into the CZTS material, within the range $0 \le x \le 1$, resulted in significant changes. Specifically, it led to a decrease in the band gap from 1.515 to 1.206 eV and an increase in the grain size from 5.97 to 27.17 nm, respectively [84]. Finally, the grain size is enhanced when the iron concentration increases in the CZTS material, especially at $x = 0.5$, as depicted in Fig. 8d. Furthermore, the high concentration of iron magnetic ions also results in particle agglomeration, as demonstrated in Fig. 8b–f.

On the other hand, Fig. 9a shows the XRD results of CZTS ($x = 0$, International Centre for Diffraction Data (ICCD) no. 01-075-4122), CFTS ($x = 1$, ICCD no. 00-035-0582) and CZFTS ($0 \le x \le 1$) thin film from the [1 1 2], [2 0 0], [2 2 0] and [3 1 2] planes. Moreover, the features are attributed to disorder effects in the mixed crystals, associated with the structural shift originating from the kesterite to the stannite crystalline structures, especially when Fe takes values of 0.5. Likewise, there were shifts in the 2θ angle with increased Fe concentrations. Fig. 9b shows that, as the concentration of Fe in the films increases, a Raman red shift is observed. Similarly, this shift is due to the modification of the Zn^{2+}(0.64 Å) for Fe^{2+}(0.66 Å). In a previous report, the spectra were analysed and characterized by using two main A1 vibrational modes from the CFTS stannite structure at 285 and 318 cm^{-1}. These modes subsequently convert into the two main A modes originating from the CZTS kesterite structure, displaying frequencies in the same range of ~287 and ~337 cm^{-1}. These analogous values are associated with the fact that the only vibrations involved in these modes are those of the S atoms [85–87].

On the other hand, the XPS results are reported in Fig. 10a–e, where the oxidation states of the CZFTS are reciprocal to Cu2p, Zn2p, Fe2p, Sn3d and S2p spectra, respectively. In addition, Fig. 10a–d shows double signals for the spectra Cu $2p_{1/2}$ (952.1 eV) and Cu $2p_{3/2}$ (932.3 eV), Zn $2p_{1/2}$ (1044.8 eV) and Zn $2p_{3/2}$ (1021.7 eV), Fe $2p_{1/2}$ (724.5 eV) and Fe $2p_{3/2}$ (710.0 eV), Sn $3d_{3/2}$ (494.6 eV) and Sn $3d_{5/2}$ (486.3 eV), S $2p_{1/2}$ (162.5 eV) and S $2p_{3/2}$ (161.7 eV) [84, 90], which also coincide with the previously reported values [74, 75, 91, 92]. Furthermore, the differences in binding energies (ΔE) corresponding to the double signals are consistent with the valence states Cu^{+1}, Zn^{+2}, Fe^{+2}, Sn^{+4} and S^{-2}, respectively. Regarding the iron-substituted and modified materials described in Table 10, most bibliographic references lack supporting information, allowing punctual comparisons. Moreover, it can be observed that most of them include sulphur atoms (CFTS) in their structure, which come from precursor compounds such as thiourea, sulphur powder or cupric sulphate [90, 94, 98–100]. In the case of $Cu_2FeSnSe_4$ (CFTSe) materials, selenium powder dissolved in oleylamine is used [87]. According to previous reports in the literature, the presence of selenium improves the efficiency and current output of the PV device [79]. However, it must be remembered that selenium is a toxic element that is more costly than sulphur and could affect the economy of scale.

On the other hand, it was reported that CFTS materials are p-type semiconductors and show a direct band gap. Likewise, it was found that only the efficiencies for three iron-substituted

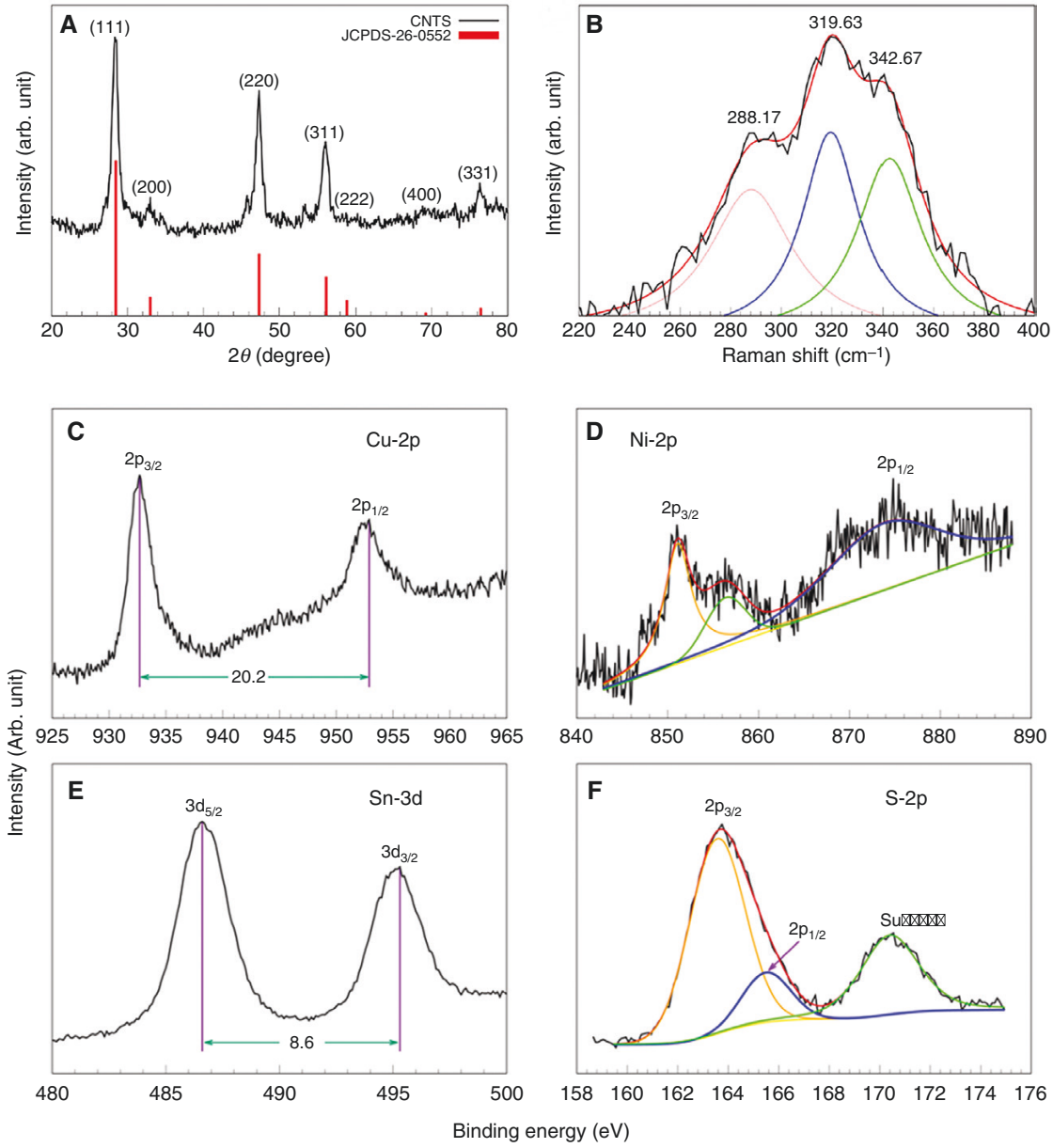

Fig 11: (a) X-ray diffraction patterns of Cu_2NiSnS_4; (b) Raman spectra of Cu_2NiSnS_4; prepared by using the hot-injection method; XPS spectrum of Cu_2NiSnS_4: (c) Cu2p; (d) Ni2p; (e) Sn3d and (f) S2p. Reproduced from [103] with permission from the American Chemical Society.

materials, namely 0.07%, 2.90% and 7.36%, respectively, are reported [90, 94, 97]. Furthermore, it could be shown that, with the increase in the sulphur concentration from 0.04 to 0.07 M thiourea, there was an improvement in mobility from 0.02×10^2 to 10.60×10^2 $cm^2V^{-1}s^{-1}$ and a reduction in electrical resistivity from 13.11 to 0.46 Ωcm, respectively [99]. Similarly, at annealing temperatures of >160°C, mobility and carrier concentration increased by 1.86×10^2 $cm^2V^{-1}s^{-1}$ and 0.74×10^{17} cm^{-3}, respectively [100]. In conclusion, sulphur ostensibly improves the calculated Hall effect coefficients, is cheap, reduces costs, is abundant in nature and is environmentally friendly.

On the other hand, the band-gap values found in this bibliographic compilation oscillate in a range of 1.05–1.87 eV. However, most of the materials referenced in Table 10 present values of ≥1.42 eV due to the substitution of the Zn^{+2} cation by Fe^{+2} in the kesterite since iron has an ionic radius of 0.77 Å and is larger than zinc, at 0.74 Å [55]. Likewise, the difference in electronegativities between Zn (1.65) and Fe (1.82) [96] significantly affects the band-gap values and, as a consequence, reduces the grain sizes of the CFTS and CFTSe materials, which vary between 0.006 and 0.6 µm, respectively. The methods used for synthesizing CFTS and CFTSe materials are very varied. However, the implementation of the hydrothermal method is not observed and therefore it has become an excellent opportunity for obtaining and documenting this type of material.

2.6 Zinc substituted by nickel in kesterite materials

The thin films of the $Cu_2(Zn_xNi_{1-x})SnS_4$ were obtained by the hydrothermal method, replacing zinc for nickel varying x from 0.0, 0.25, 0.50, 0.75 to 1.0, in the CZTS material, respectively [102]. In addition, the crystalline phases were analysed by using XRD patterns, confirming a gradual shift peak [1 1 2] to [1 1 1] in the crystal plane when the nickel concentration increases. Moreover,

Table 11: Optoelectronic parameters measured on nickel thin-film absorber materials

Substituent element	Material	Type	n (cm^{-3})	μ ($cm^2 V^{-1} s^{-1}$)	E_g	V_{oc} (V)	J_{sc} (mA cm^{-2})	FF (%)	PCE (%)	Grain size (μm)	Method	Year	Source
Ni	Cu_2NiSnS_4	p	–	–	1.56	–	–	–	–	0.02	Hydrothermal	2015	[107]
Ni	Cu_2NiSnS_4	–	–	–	1.74	–	–	–	–	–	Sol–gel/ spin-coating	2016	[95]
Ni	Cu_2NiSnS_4	p	–	–	1.57	0.423	0.52	0.43	0.09	0.012	Hot injection	2017	[103]
Ni	$Cu_2Zn_xNi_{1-x}SnS_4$	p	–	–	1.36	–	–	–	–	0.012	Hydrothermal	2017	[102]
Ni	$Cu_2NiSnSe_4$	–	–	–	1.39	–	–	–	–	0.005	Wet chemical heating up	2018	[87]
Ni	Cu_2NiSnS_4	–	–	–	1.95	0.670	16.74	0.73	8.20	–	Density functional theory	2018	[108]
Ni	Cu_2NiSnS_4	p	4.5×10^{17}	3.0	1.35	–	–	–	–	–	Sol–gel	2020	[109]
Ni	Cu_2NiSnS_4	p				0.750	14.36	0.670	7.20		Hydrothermal	2022	[110]
Ni	Cu_2NiSnS_4/ EEG	p				0.743	16.12	0.662	7.92		Hydrothermal	2022	[110]

the ionic radius of nickel (690 Å) is less than that of zinc (740 Å), reducing the lattice constants. This reduction leads to the displacement of the diffraction peak to a higher angle [102]. Furthermore, Fig. 11a depicts the original JCPDS data card of the Cu_2NiSnS_4—26-0552, which matches the experimental results. Likewise, Cu_2NiSnS_4 shows peaks of $2\theta = 28.50°$, 33.03°, 47.35°, 56.11°, 58,80°, 69.04° and 76.31°, which means the crystal planes of [1 1 1], [2 0 0], [2 2 0], [3 1 1], [2 2 2], [4 0 0] and [3 3 1], respectively [103]. Moreover, the diffraction pattern peaks [1 1 1], [2 0 0], [2 2 0] and [3 1 1] constitute the stannite structure. Fig. 11b shows the Raman spectroscopy of the Cu_2NiSnS_4 (CNTS) material, where the red line represents the most significant peaks that were summed and fitted (342.67, 319.63 and 288.17 cm^{-1}). In addition, no secondary phases were detected.

Similarly, Raman spectra of $Cu_2Zn_xNi_{1-x}SnS_4$ showed high intensity in the range of 330 to 338 cm^{-1}. Previous studies have indicated a correlation with the A1 symmetry mode Raman, particularly with peak positions at 331 and 338 cm^{-1} of CZTS [95, 102, 104, 105]. $Cu_2Zn_xNi_{1-x}SnS_4$ nanoparticles exhibit a slight red shift of ~2–5 cm^{-1} due to Ni^{2+} ions being incorporated into the Zn^{2+} lattice sites. In addition, the Raman peaks of secondary phases, such as SnS (192 cm^{-1}) and SnS_2 (314 cm^{-1}), do not appear in the Raman spectra of $Cu_2Zn_xNi_{1-x}SnS_4$ (x = 0), indicating the presence of a stannite crystal structure. Furthermore, no other secondary phases, namely ZnS (351 cm^{-1}), Cu_3SnS_4 (318 cm^{-1}) and Cu_2SnS_3 (298 cm^{-1}), are observed, confirming the existence of the crystal structures of kesterite and stannite, both in their pure single-phase form [85, 102]. Concerning XPS, Fig. 11c–f represents core levels of Cu2p, Ni2p, Sn3d and S2p species. In addition, double signals for the spectra Cu $2p_{1/2}$ (951.10 eV) and Cu $2p_{3/2}$ (930.97 eV), Ni $2p_{3/2}$ (854.80 eV) and Ni $2p_{3/2}$ (859.18 eV Sat), Sn $3d_{3/2}$ (493.85 eV) and Sn $3d_{5/2}$ (485.31 eV), S $2p_{1/2}$ (160.38 eV) and S $2p_{3/2}$ (167.03 eV) are shown, which also coincide with the previously reported values [74, 75, 91, 106]. Likewise, the differences in binding energies (ΔE) corresponding to the double signals are consistent with the valence states Cu^{+1}, Ni^{+2}, Sn^{+4} and S^{-2}, respectively.

On the other hand, Table 11 summarizes the Cu_2NiSnS_4 (CNTS) thin-film materials synthesized by using different methods and whose optoelectronic properties are reported showing the following characteristics: p-type conductivities, carrier concentration 4.5×10^{17} cm^{-3}, resistivity 0.4 Ω cm, band gap 1.35 eV and absorption coefficients of $>10^4$ cm^{-1} [109]. Similarly, CNTS materials were synthesized using a hydrothermal method with water as the reaction medium. This research revealed positive values for the Seebeck coefficient, indicating p-type conductivity. The sample exhibited an activation energy of 160 meV and a band gap of 1.56 eV, suggesting favourable conditions for PV applications [107]. Similarly, the $Cu_2Zn_xNi_{1-x}SnS_4$ material was synthesized via the hydrothermal method, with the nickel concentration varied from x = 0.0, 0.25, 0.5, 0.75 up to 1.0, respectively. It was found that the total or partial substitution of Zn by Ni contributed to increased electrical conductivity and reduced the band gap from 1.63 eV (x = 1.0) to 1.36 eV (x = 0.0). This effect is due to the hybridization of Ni (3d) and S (3p) in preferred orbitals within the $Cu_2Zn_xNi_{1-x}SnS_4$ pentanary nanoparticle system [102]. However, the average crystal size in the CZTS system decreased as the nickel content increased, ranging from 40 to 12 nm, respectively. According to a previous report, there is an inverse relationship between the band gap and the particle size, and, according to Table 11, the particle sizes are in the range of 0.005–0.02 μm, which justifies the high band-gap values referenced and a possible decrease in the efficiency of the PV devices [65].

On the contrary, DFT calculations demonstrated that the CNTS material exhibited an improved efficiency of 8.2% compared with the starting material CZTS, which had an efficiency of 7.9% in dye-sensitized solar cell (DSSCs). This improvement was attributed to a band gap of 1.95 eV [108]. However, the experimental results obtained using the hydrothermal method for the pristine materials Cu_2NiSnS_4 and $Cu_2NiSnSnS_4$/graphene hybrid showed efficiencies of 7.20% and 7.92%, respectively. These findings corroborate the agreement between the calculated theoretical data and the experimental results, and justify using nickel as a zinc substituent [110].

In conclusion, different methods have been used to obtain CNTS materials by substituting Zn cations for Ni, showing that the band gap decreases as the nickel concentrations increase in the CZTS material. However, the referenced values range between 1.35 and 1.95 eV, mainly due to the proportions handled between Cu, Ni, Sn and S for each study method. It was also found that, with increasing nickel concentrations, the grain sizes obtained were ≤0.02 μm, which had a notable influence on the performance of the PV cell. However, other properties show significant improvements, such as decreased resistivity and increased conductivity, concentration carriers and absorption coefficients.

Finally, the literature references consulted lack relevant information and leave gaps when looking for points of comparison in the synthesis of CNTS materials.

3 Conclusions

Renewable energies could be an alternative to substitute fossil fuels and contribute to mitigating greenhouse gas emissions. However, the installed capacity in the world is low compared with other conventional energy types. Thin-film devices that convert solar energy into electrical energy have shown promising results but still need improvement. One clear example of achieving optimal performance in PV devices is introducing alkaline modifiers into kesterite lattice structures.

The best result was found using a lithium-like metal modifier of kesterite materials and this can be attributed to the close ionic radius of Li^+ (0.73 Å) compared with Cu^+ (0.74 Å) and Zn^{2+} (0.74 Å). Despite a reduction in carrier density caused by certain Li atoms taking up positions in V_{Cu}, the materials modified using Li maintain a relatively high carrier density (1.4×10^{15} cm^{-3}) compared with other materials modified using K, Na, Rb and Cs, with studied values of 9.9×10^{14}, 6.8×10^{14}, 5.6×10^{14} and 4.8×10^{14} cm^{-3}, respectively. On the other hand, the alkaline earth metals, when acting as substituents for Zn and not as extrinsic modifiers of the CZTS absorber material, presented low energy efficiency conversions. That can be attributed to the mismatches of ionic radii between Zn regarding Ca, Ba and Sr, which create antisite defects and variations in optoelectronic properties. Concerning Mg as a modifier in thin-film materials, it is crucial to highlight the absence of secondary phases identified through XRD and Raman analysis. Additionally, it does not affect the crystalline structure of the CZTS material, reducing the number of structural defects and tuning the band gaps. Furthermore, the Mg content contributes to increased lattice constants, improved grain growth and enhanced optoelectronic properties.

On the other hand, another crucial finding is the identification of carbon impurities in CZTS and CZMTS PV materials, which arise from the decomposition of organic solvents during the synthesis process. However, by introducing an Mg-like modifier into CZMTS, the carbon content decreases, leading to a slight improvement in the efficiency of the CZMTS cell. Furthermore, using selenium in Mg-modified kesterite materials improves the efficiency of PV cells. However, trace selenium is essential for human health but is harmful at high concentrations (400 µg/day).

On the other hand, regarding iron substitution, when the concentration of this metal increases in the CZTS material, the grain size decreases significantly, affecting the optoelectronic properties of the produced CFTS materials. Likewise, Raman spectra show a red shift as the Fe concentration in the thin films increases and promotes the conversion of kesterite into the stannite phase. Regarding the stoichiometric ratio of CFTS, minimal sulphur content (≤0.06M) improves the absorption coefficient tuning band gap and reduces the resistivity values of thin-film materials produced.

However, different methods have been used to obtain CNTS materials by substituting Zn cations for Ni, showing that the band gap decreases as the nickel concentrations increase in the CZTS material. Nevertheless, the band-gap range variation is mainly due to the proportions handled between Cu, Ni, Sn and S for each study method. It was also found that, as nickel concentrations increase, the grain sizes obtained are ≤0.02 µm, significantly affecting the performance of the PV cell. However, several other properties have improved considerably, including decreased resistivity, increased conductivity, higher carrier concentration and enhanced absorption coefficients. Additionally, it has been discovered that the total or partial substitution of Zn with Ni contributes to increased electrical conductivity and decreases the band gap of the $Cu_2Zn_{1-x}Ni_xSnS_4$ (CZNTS) pentanary nanoparticle system. To conclude, CZTS material modified with alkali metals, transition metals or alkali earth metals improves energy conversion efficiency (PCE) and other optoelectronic properties but substitution with the same metals decreases efficiency and the grain size and increases the band gap.

Acknowledgements

National Learning Service (SENA), Mining Center, Sogamoso, Colombia; Group of Integrity and Evaluation of Materials (GIEM) at the Pedagogical and Technological University of Colombia, Tunja, Colombia; Research Group of Inorganic and Organic Chemistry at the University Jaume I of Castellón de la Plana (Spain).

Author contributions

NE and JG contributed to conceptualization; EV, JC and JG contributed to validation; NE contributed to the investigation; NE and JG contributed to writing–original draft; NE, JG and JC contributed to writing–review and editing; EV, JC and JG contributed to supervision and project administration.

Conflict of interest statement

The authors declare that they have no conflict of interest.

References

[1] Nayak PK, Mahesh S, Snaith HJ, *et al*. Photovoltaic solar cell technologies: analysing the state of the art. *Nat Rev Mater*, 2019, 4:269–285. https://doi.org/10.1038/s41578-019-0097-0

[2] IEA. *Renewables 2021, Analysis and forecast to 2026*. International Energy Agency (IEA) Publications International, 2021. https://iea.blob.core.windows.net/assets/5ae32253-7409-4f9a-a91d-1493ffb9777a/Renewables2021-AnalysisandforecasttoIEA2026.pdf (16 November 2023, date last accessed).

[3] Nazligul A, Wang M, Choy KL. Recent development in earth-abundant kesterite materials and their applications. *Sustainability*, 2020, 12:5138. https://doi.org/10.3390/su12125138

[4] Liu F, Zeng Q, Li J, *et al*. Emerging inorganic compound thin film photovoltaic materials: progress, challenges and strategies. *Mater Today*, 2020, 41:120–142. https://doi.org/10.1016/j.mattod.2020.09.002

[5] Feurer T, Reinhard P, Avancini E, *et al*. Progress in thin film CIGS photovoltaics: research and development, manufacturing, and applications. *Prog Photovolt Res Appl*, 2016, 25:645–667. https://doi.org/10.1002/pip.2811

[6] Lee T, Ebong A. Thin film solar cell technologies and challenges: a review. *Renew Sustain Energy Rev*, 2017, 70:1286–1212. https://doi.org/10.1016/j.rser.2016.12.028

[7] Delbos S. Këwhile terite thin films for photovoltaics: a review. *EPJ Photovolt*, 2012, 3:35004. https://doi.org/10.1051/epjpv/2012008

[8] Kasap S, Capper P. *Springer Handbook of Electronic and Photonic Materials*. 1st edn. New York: Springer, 2006. https://doi.org/10.1007/978-0-387-29185-7

[9] Grossberg M, Krustok J, Hages CJ, *et al*. The electrical and optical properties of kesterites. *J Phys Energy*, 2019, 1:044002. https://doi.org/10.1088/2515-7655/ab29a0

[10] Guo Y, Wang Q, Kawazoe Y, *et al*. A new silicon phase with direct band gap and novel optoelectronic properties. *Sci Rep*, 2015, 5:14342. https://doi.org/10.1038/srep14342

[11] Martí Valls R. Obtención de estructuras calcopirita (CIGS) y kesterita (CZTS) como absorbedores para dispositivos fotovoltaicos de capa fina mediante métodos de síntesis de bajo coste. *Ph.D. thesis*. Universidad Jaume I, Castellon de la Plana, España, 2016. http://hdl.handle.net/10803/400856

[12] Richter A, Hermle M, Glunz SW. Reassessment of the limiting efficiency for crystalline silicon solar cells. *IEEE J Photovolt*, 2013, 3:1184–1191. https://doi.org/10.1109/JPHOTOV.2013.2270351

[13] Green M, Dunlop E, Hohl-Ebinger J, *et al*. Solar cell efficiency tables (Version 55). *Prog Photovolt Res Appl*, 2020, 28:3–15. https://doi.org/10.1002/pip.3228

[14] Wang W, Winkler MT, Gunawan O, *et al*. Device characteristics of CZTSSe thin-film solar cells with 126% efficiency. *Adv Energy Mater*, 2014, 4:1301465. https://doi.org/10.1002/aenm.201301465

[15] Barrionuevo González JJ. Síntesis y caracterización de Cu_2ZnSnS_4 impurificado con Se para aplicaciones en celdas solares. *M.Sc. thesis*. Universidad de Ciencias y Artes de Chiapas, Tuxtla Gutiérrez, 2015. https://repositorio.unicach.mx/handle/20.500.12753/708?show=full%0A (16 November 2023, date last accessed).

[16] Hurtado-Morales M. Síntesis y caracterización de películas delgadas del semiconductor Cu_2ZnSnS_4 y su uso como capa absorbente en celdas solares. *Ph.D.thesis*. Universidad Nacional de Colombia, Bogotá, Colombia, 2014. https://repositorio.unal.edu.co/handle/unal/52170 (16 November 2023, date last accessed).

[17] Fontané X, Calvo-Barrio L, Izquierdo-Roca V, *et al*. In-depth resolved Raman scattering analysis for the identification of secondary phases: characterization of Cu_2ZnSnS_4 layers for solar cell applications. *Appl Phys Lett*, 2011, 98:181905. https://doi.org/10.1063/1.3587614

[18] Maeda T, Nakamura S, Wada T. First principles calculations of defect formation in in-free photovoltaic semiconductors Cu_2ZnSnS_4 and $Cu_2ZnSnSe_4$. *Thin Solid Films*, 2011, 519:7513–7516. https://doi.org/10.1016/j.tsf.2011.01.094

[19] Hurtado M. Preparation and characterization of $Cu_2ZnSnSe_4$ thin films grown from ZnSe and Cu_2SnS_3 precursors in a two stage process. *Rev Elem*, 2012, 2:117–131. https://doi.org/10.1088/1742-6596/480/1/012007

[20] Lie S, Leow S, Bishop DM, *et al*. Improving carrier-transport properties of CZTS by Mg incorporation with spray pyrolysis. *ACS Appl Mater Interfaces*, 2019, 11:25824–25832. https://doi.org/10.1021/acsami.9b05244

[21] Zhang X, Fu E, Zheng M, *et al*. Fabrication of Cu_2ZnSnS_4 thin films from ball-milled nanoparticle inks under various annealing temperatures. *Nanomaterials*, 2019, 9:1615. https://doi.org/10.3390/nano9111615

[22] Siebentritt S, Schorr S. Kesterites—a challenging material for solar cells. *Prog Photovolt Res Appl*, 2012, 20:512–519. https://doi.org/10.1002/pip.2156

[23] Kumar M, Dubey A, Adhikari N, *et al*. Strategic review of secondary phases, defects and defect-complexes in kesterite CZTS-Se solar cells. *Energy Environ Sci*, 2015, 8:3134–3159. https://doi.org/10.1039/c5ee02153g

[24] Chen S, Walsh A, Gong XG, *et al*. Classification of lattice defects in the kesterite Cu_2ZnSnS_4 and $Cu_2ZnSnSe_4$ earth-abundant solar cell absorbers. *Adv Mater*, 2013, 25:1522–1539. https://doi.org/10.1002/adma.201203146

[25] Fontané Sánchez X. Caracterización por espectroscopia Raman de semiconductores Cu_2ZnSnS_4 para nuevas tecnologías fotovoltaicas. *Ph.D. thesis*. Universidad de Barcelona, Barcelona, España, 2013. http://hdl.handle.net/2445/54689%0A (16 November 2023, date last accessed).

[26] Schorr S, Gurieva G, Guc M, *et al*. Point defects, compositional fluctuations, and secondary phases in non-stoichiometric kesterites. *J Phys Energy*, 2019, 2:012002. https://doi.org/10.1088/2515-7655/ab4a25

[27] Wang Y, Hao R, Guo J, *et al*. Effect of Mg doping on Cu2ZnSnS4 solar cells prepared by DMF-based solution method. *Opt Mater*, 2021, 117:111211. https://doi.org/10.1016/j.optmat.2021.111211

[28] Lin X. Solution processed $Cu_2ZnSn(S_xSe_{1-x})_4$ thin films based on binary and ternary chalcogenide nanoparticle precursors and their application in solar cells. *Ph.D. thesis*. Technical University of Berlin, Germany, 2013. https://depositonce.tu-berlin.de/bitstreams/3b7d5844-9ffe-43b8-8a2c-7c33253bc2b4/download (16 November 2023, date last accessed).

[29] Olgar MA, Tomakin MU, Kucukomeroglu T, *et al*. Growth of Cu_2ZnSnS_4 (CZTS) thin films using short sulfurization periods. *Mater Res Express*, 2019, 6:056401. https://doi.org/10.1088/2053-1591/aaff78

[30] Kim J, Shin B. Strategies to reduce the open-circuit voltage deficit in $Cu_2ZnSn(S,Se)_4$ thin film solar cells. *Electron Mater Lett*, 2017, 13:373–392. https://doi.org/10.1007/s13391-017-7118-1

[31] Enayati M, Mohammadnejad S. Reduction of interface recombination current for higher performance of p+-CZT(S_xSe_{1-x})/p-CZTS/n-CdS thin-film solar cells using Kesterite intermediate layers. *Sol Energy*, 2020, 204:489–500. https://doi.org/10.1016/j.solener.2020.04.096

[32] Enayati M, Mohammadnejad S. Enhancing the open-circuit voltage and efficiency of CZTS thin-film solar cells via band-offset engineering. *Opt Quantum Electron*, 2020, 52:72. https://doi.org/10.1007/s11082-019-2180-6

[33] Lee Y, Gershon T, Gunawan O, *et al*. $Cu_2ZnSnSe_4$ thin-film solar cells by thermal co-evaporation with 116% efficiency and improved minority carrier diffusion length. *Adv Energy Mater*, 2015, 5:1401372. https://doi.org/10.1002/aenm.201401372

[34] Tajima S, Umhejara M, Hasegawa M, *et al*. Cu_2ZnSnS_4 photovoltaic cell with improved efficiency fabricated by high-temperature annealing after CdS buffer-layer deposition. *Prog Photovolt Res Appl*, 2016, 25:14–22. https://doi.org/10.1002/pip.2837

[35] Romanyuk YE, Haass SG, Giraldo S, *et al*. Doping and alloying of kesterites. *J Phys Energy*, 2019, 1:044004. https://doi.org/10.1088/2515-7655/ab23bc

[36] Hsieh Y, Han Q, Jiang C, *et al*. Efficiency enhancement of $Cu_2ZnSn(S,Se)_4$ solar cells via Alkali metals doping. *Adv Energy Mater*, 2016, 6:1502386. https://doi.org/10.1002/aenm.201502386

[37] Kim J, Larina L, Chung CY, *et al*. Atomistic consideration of earth-abundant chalcogenide materials for photovoltaics: kesterite and beyond. *J Mater Res*, 2018, 33:3986–3998. https://doi.org/10.1557/jmr.2018.350

[38] Li S, Lloyd M, McCandless BE, *et al*. Effects of cation composition on carrier dynamics and photovoltaic performance in $Cu_2ZnSnSe_4$ monocrystal solar cells. *Sol Energy Mater Sol Cells*, 2020, 205:110255. https://doi.org/10.1016/j.solmat.2019.110255

[39] Duan B, Guo L, Yu Q, *et al*. Highly efficient solution-processed CZTSSe solar cells based on a convenient sodium-incorporated post-treatment method. *J Energy Chem*, 2020, 40:196–203. https://doi.org/10.1016/j.jechem.2019.03.029

[40] Haass S, Andres C, Figi R, *et al*. Complex interplay between absorber composition and alkali doping in high-efficiency kesterite solar cells. *Adv Energy Mater*, 2018, 8:1701760. https://doi.org/10.1002/aenm.201701760

[41] Xu X, Qu Y, Campbell S, *et al*. Solution processing route to Na incorporation in CZTSSe nanoparticle ink solar cells on foil substrate. *J Mater Sci Mater Electron*, 2019, 30:7883–7889. https://doi.org/10.1007/s10854-019-01108-3

[42] Li W, Su Z, Tan JMR, *et al*. Revealing the role of potassium treatment in CZTSSe thin film solar cells. *Chem Mater*, 2017, 29:4273–4281. https://doi.org/10.1021/acs.chemmater.7b00418

[43] Altamura G, Wang M, Choy KL. Influence of alkali metals (Na, Li, Rb) on the performance of electrostatic spray-assisted vapor deposited $Cu_2ZnSn(S,Se)_4$ solar cells. *Sci Rep*, 2016, 6:22109. https://doi.org/10.1038/srep22109

[44] Mlotshwa T. Density functional theory study of copper zinc tin sulphide (Cu_2ZnSnS_4) doped with calcium and barium. University of Venda, Thohoyandou, Sudafrica, 2020. http://hdl.handle.net/11602/1665%0A (16 November 2023, date last accessed).

[45] Berman S, Sai Gautam G, Carter EA. Role of Na and Ca as isovalent dopants in Cu_2ZnSnS_4 solar cells. *ACS Sustain Chem Eng*, 2019, 7:5792–5800. https://doi.org/10.1021/acssuschemeng.8b05348

[46] Chen R, Persson C. Electronic and optical properties of Cu_2XSnS_4 (X = Be, Mg, Ca, Mn, Fe, and Ni) and the impact of native defect pairs: a review. *J Appl Phys*, 2017, 121:203104. https://doi.org/10.1063/1.4984115

[47] Li J, Wang D, Li X, *et al*. Cation substitution in earth-abundant kesterite photovoltaic materials. *Adv Sci*, 2018, 5:1700744. https://doi.org/10.1002/advs.201700744

[48] Hong F, Lin W, Meng W, *et al*. Trigonal $Cu_2IISnVI_4$ (II = Ba, Sr and VI = S, Se) quaternary compounds for earth-abundant photovoltaics. *Phys Chem Chem Phys*, 2016, 18:4828–4834. https://doi.org/10.1039/c5cp06977g

[49] Yang G, Zhai X, Li Y, *et al*. Synthesis and characterizations of Cu_2MgSnS_4 thin films with different sulfuration temperatures. *Mater Lett*, 2019, 242:58–61. https://doi.org/10.1016/j.matlet.2019.01.102

[50] Ge J, Yan Y. Synthesis and characterization of photoelectrochemical and photovoltaic Cu_2BaSnS_4 thin films and solar cells. *J Mater Chem C*, 2017, 5:6406–6419. https://doi.org/10.1039/c7tc01678f

[51] Shin D, Zhu T, Huang X, *et al*. Earth-abundant chalcogenide photovoltaic devices with over 5% efficiency based on a $Cu_2BaSn(S,Se)_4$ absorber. *Adv Mater*, 2017, 29:1606945. https://doi.org/10.1002/adma.201606945

[52] Ge J, Koirala P, Grice CR, *et al*. Oxygenated CdS buffer layers enabling high open-circuit voltages in earth-abundant Cu_2BaSnS_4 thin-film solar cells. *Adv Energy Mater*, 2017, 7:1601803. https://doi.org/10.1002/aenm.201601803

[53] Xiao H, Chen Z, Sun K, *et al*. Sol-gel solution-processed Cu_2SrSnS_4 thin films for solar energy harvesting. *Thin Solid Films*, 2020, 697:137828. https://doi.org/10.1016/j.tsf.2020.137828

[54] Crovetto A, Nielsen R, Stamate E, *et al*. Wide band gap Cu_2SrSnS_4 solar cells from oxide precursors. *ACS Appl Energy Mater*, 2019, 2:7340–7344. https://doi.org/10.1021/acsaem.9b01322

[55] Tian Q, Liu S. Defect suppression in multinary chalcogenide photovoltaic materials derived from kesterite: progress and outlook. *J Mater Chem A*, 2020, 8:24920–24942. https://doi.org/10.1039/d0ta08202c

[56] Yan C, Huang J, Sun K, *et al*. Cu_2ZnSnS_4 solar cells with over 10% power conversion efficiency enabled by heterojunction heat treatment. *Nat Energy*, 2018, 3:764–772. https://doi.org/10.1038/s41560-018-0206-0

[57] Sharma A, Sahoo P, Singha A, *et al*. Efficient visible-light-driven water splitting performance of sulfidation-free, solution processed Cu_2MgSnS_4 thin films: role of post-drying temperature. *Sol Energy*, 2020, 203:284–295. https://doi.org/10.1016/j.solener.2020.04.027

[58] Wei M, Du Q, Wang R, *et al*. Synthesis of new earth-abundant kesterite Cu_2MgSnS_4 nanoparticles by hot-injection method. *Chem Lett*, 2014, 43:1149–1151. https://doi.org/10.1246/cl.140208

[59] Pavan Kumar V, Guilmeau E, Raveau B, *et al*. A new wide band gap thermoelectric quaternary selenide $Cu_2MgSnSe_4$. *J Appl Phys*, 2015, 118:155101. https://doi.org/10.1063/1.4933277

[60] Guo Y, Cheng W, Jiang J, *et al*. The structural, morphological and optical-electrical characteristic of Cu_2XSnS_4 (X:Cu,Mg) thin films fabricated by novel ultrasonic co-spray pyrolysis. *Mater Lett*, 2016, 172:68–71. https://doi.org/10.1016/j.matlet.2016.02.088

[61] Souli M, Engazou R, Ajili L, *et al*. Physical properties evolution of sprayed Cu_2MgSnS_4 thin films with growth parameters and vacuum annealing. *Superlattices Microstruct*, 2020, 147:106711. https://doi.org/10.1016/j.spmi.2020.106711

[62] Odin I, Gapanovich M, Urkhanov OY, *et al*. Crystallographic and luminescence characteristics of the $Cu_2MgSnSe_4$ quaternary compound and $Cu_{2-x}MgSnSe_4$ ($0 < x \leq 015$) copper-deficient solid solutions. *Inorg Mater*, 2021, 57:3–9. https://doi.org/10.1134/S0020168521010118

[63] Hammoud A, Jrad A, Yahmadi B, *et al*. Investigation on Cu_2MgSnS_4 thin film prepared by spray pyrolysis for photovoltaic and humidity sensor applications. *Opt Mater*, 2022, 127:112296. https://doi.org/10.1016/j.optmat.2022.112296

[64] Zhong G, Tse K, Zhang Y, *et al*. Induced effects by the substitution of Zn in Cu_2ZnSnX_4 (X = S and Se). *Thin Solid Films*, 2016, 603:224–229. https://doi.org/10.1016/j.tsf.2016.02.005

[65] Maldar P, Gaikwad M, Mane AA, *et al*. Fabrication of Cu_2CoSnS_4 thin films by a facile spray pyrolysis for photovoltaic application. *Sol Energy*, 2017, 158:89–99. https://doi.org/10.1016/j.solener.2017.09.036

[66] Mena Romero DM, Victoria Valenzuela D, Azanza Ricardo CL. Partial and total substitution of Zn by Mg in the Cu_2ZnSnS_4 structure. *Crystals*, 2020, 10:578. https://doi.org/10.3390/cryst10070578

[67] Wang Y, Yang Y, Zhu C, *et al*. Boosting the electrical properties of $Cu_2ZnSn(S,Se)_4$ solar cells via low amounts of Mg substituting Zn. *ACS Appl Energy Mater*, 2020, 3:11177–11182. https://doi.org/10.1021/acsaem.0c02121

[68] Kuo D, Wubet W. Mg dopant in $Cu_2ZnSnSe_4$: an n-type former and a promoter of electrical mobility up to 120 $cm^2V^{-1}s^{-1}$. *J Solid State Chem*, 2014, 215:122–127. https://doi.org/10.1016/j.jssc.2014.03.034

[69] Agawane G, Vanalakar S, Kamble AS, *et al*. Fabrication of $Cu_2(Zn_xMg_{1-x})SnS_4$ thin films by pulsed laser deposition technique for solar cell applications. *Mater Sci Semicond Process*, 2018, 76:50–54. https://doi.org/10.1016/j.mssp.2017.12.010

[70] Caballero R, Haass SG, Andres C, *et al*. Effect of magnesium incorporation on solution-processed kesterite solar cells. *Front Chem*, 2018, 6:5. https://doi.org/10.3389/fchem.2018.00005

[71] Wang C, Chen S, Yang YH, *et al*. Design of I_2-II-IV-VI_4 semiconductors through element substitution: the thermodynamic stability limit and chemical trend. *Chem Mater*, 2014, 26:3411–3417. https://doi.org/10.1021/cm500598x

[72] Sui Y, Zhang Y, Jiang D, *et al*. Investigation of optimum Mg doping content and annealing parameters of $Cu_2(Mg_xZn_{1-x})SnS_4$ thin films for solar cells. *Nanomaterials*, 2019, 9:955. https://doi.org/10.3390/nano9070955

[73] Guo W, Ding K, Mei S, *et al*. Hollow spheres consisting of SnS nanosheets conformally coated with S-doped carbon for advanced lithium-/sodium-ion battery anodes. *ChemElectroChem*, 2020, 7:875–875. https://doi.org/10.1002/celc.201901923

[74] Calderón C, Gordillo G, Becerra R, *et al*. XPS analysis and characterization of thin films Cu_2ZnSnS_4 grown using a novel solution based route. *Mater Sci Semicond Process*, 2015, 39:492–498. https://doi.org/10.1016/j.mssp.2015.05.064

[75] Liu W, Guo B, Wu XS, *et al*. Facile hydrothermal synthesis of hydrotropic Cu_2ZnSnS_4 nanocrystal quantum dots: band-gap engineering and phonon confinement effect. *J Mater Chem A*, 2013, 1:3182–3186. https://doi.org/10.1039/c3ta00357d

[76] Jiang D, Zhang Y, Sui Y, *et al*. Investigation on the selenization treatment of kesterite $Cu_2Mg_{0.2}Zn_{0.8}Sn(S,Se)_4$ films for solar cell. *Nanomaterials*, 2019, 9:946. https://doi.org/10.3390/nano9070946

[77] Cho J, Ismail A, Park SJ, *et al*. Synthesis of Cu_2ZnSnS_4 thin films by a precursor solution paste for thin film solar cell applications. *ACS Appl Mater Interfaces*, 2013, 5:4162–4165. https://doi.org/10.1021/am401210w

[78] Su Z, Sun K, Han Z, *et al*. Fabrication of Cu_2ZnSnS_4 solar cells with 51% efficiency via thermal decomposition and reaction using a non-toxic sol-gel route. *J Mater Chem A*, 2014, 2:500–509. https://doi.org/10.1039/c3ta13533k

[79] Kumar A. Impact of selenium composition variation in CZTS solar cell. *Optik*, 2021, 234:166421. https://doi.org/10.1016/j.ijleo.2021.166421

[80] Asensio M, Abás E, Pinilla JL, *et al*. High recovery of selenium from kesterite-based photovoltaic cells. *Eur J Inorg Chem*, 2020, 2020:2203–2209. https://doi.org/10.1002/ejic.202000261

[81] Macías López M. Síntesis, estudio estructural y propiedades magnéticas de nuevos materiales pertenecientes a los sistemas Cu_2-II-Sn-VI_4(II = Fe, Mn y VI = S, Se) Y Ba-Ce-Mn-O. *Ph.D. thesis*. Universidad Industrial de Santander, Bucaramanga, Colombia, 2014. https://noesis.uis.edu.co/handle/20.500.14071/9652%0A (16 November 2023, date last accessed).

[82] Gui Z, Fan R, Chen X, *et al*. A new colloidal precursor cooperative conversion route to nanocrystalline quaternary copper sulfide. *Mater Res Bull*, 2004, 39:237–241. https://doi.org/10.1016/j.materresbull.2003.09.035

[83] Waluś E, Manecki M, Cios G. Synthesis and characterization of Cu_2FeSnS_4- Cu_2MnSnS_4 solid solution microspheres. *Materials*, 2020, 13:4440. https://doi.org/10.3390/ma13194440

[84] Shadrokh Z, Yazdani A, Eshghi H. Solvothermal synthesis of $Cu_2Zn_{1-x}Fe_xSnS_4$ nanoparticles and the influence of annealing conditions on drop-casted thin films. *Semicond Sci Technol*, 2016, 31:045004. https://doi.org/10.1088/0268-1242/31/4/045004

[85] Fontané X, Izquierdo-Roca V, Saucedo E, *et al*. Vibrational properties of stannite and kesterite type compounds: Raman scattering analysis of $Cu_2(Fe,Zn)SnS_4$. *J Alloys Compd*, 2012, 539:190–194. https://doi.org/10.1016/j.jallcom.2012.06.042

[86] Agawane GL, Shin SW, Vanalakar SA, *et al*. Next generation promising $Cu_2(Zn_xFe_{1-x})SnS_4$ photovoltaic absorber material prepared by pulsed laser deposition technique. *Mater Lett*, 2014, 137:147–149. https://doi.org/10.1016/j.matlet.2014.08.118

[87] Dehghani Z, Shadrokh Z. Structural and optical properties of Cu_2M(M: Zn, Fe, Co, Ni)$SnSe_4$ nanoparticles synthesized via heating up method. *Optik*, 2018, 169:242–248. https://doi.org/10.1016/j.ijleo.2018.05.052

[88] Bai J, Ji J, Hao L, *et al*. DFT investigation on the electronic, magnetic, mechanical properties and strain effects of the quaternary compound Cu_2FeSnS_4. *Crystals*, 2020, 10:509. https://doi.org/10.3390/cryst10060509

[89] Trifiletti V, Tseberlidis G, Colombo M, *et al*. Growth and characterization of $Cu_2Zn_{1-x}Fe_xSnS_4$ thin films for photovoltaic applications. *Materials (Basel)*, 2020, 13:1471. https://doi.org/10.3390/ma13061471

[90] Chatterjee S, Pal A. A solution approach to p-type Cu_2FeSnS_4 thin-films and pn-junction solar cells: role of electron selective materials on their performance. *Sol Energy Mater Sol Cells*, 2017, 160:233–240. https://doi.org/10.1016/j.solmat.2016.10.037

[91] Tahir D, Tougaard S. Electronic and optical properties of Cu, CuO and Cu_2O studied by electron spectroscopy. *J Phys: Condens Matter*, 2012, 24:175002. https://doi.org/10.1088/0953-8984/24/17/175002

[92] Yamashita T, Hayes P. Analysis of XPS spectra of Fe^{2+} and Fe^{3+} ions in oxide materials. *Appl Surf Sci*, 2008, 254:2441–2449. https://doi.org/10.1016/j.apsusc.2007.09.063

[93] Ozel F, Kus M, Yar A, *et al*. Fabrication of quaternary Cu_2FeSnS_4 (CFTS) nanocrystalline fibers through electrospinning technique. *J Mater Sci*, 2014, 50:777–783. https://doi.org/10.1007/s10853-014-8637-x

[94] Meng X, Deng H, He J, *et al*. Synthesis, structure, optics and electrical properties of Cu_2FeSnS_4 thin film by sputtering metallic precursor combined with rapid thermal annealing sulfurization process. *Mater Lett*, 2015, 151:61–63. https://doi.org/10.1016/j.matlet.2015.03.046

[95] Ghosh A, Biswas A, Thangavel R, *et al*. Photo-electrochemical properties and electronic band structure of kesterite copper chalcogenide Cu_2-II-Sn-S_4 (II = Fe, Co, Ni) thin films. *RSC Adv*, 2016, 6:96025–96034. https://doi.org/10.1039/c6ra15700a

[96] Hannachi A, Oueslati H, Khemiri N, *et al*. Effects of sulfurization on the optical properties of $Cu_2Zn_xFe_{1-x}SnS_4$ thin films. *Opt Mater*, 2017, 72:702–709. https://doi.org/10.1016/j.optmat.2017.07.031

[97] Mokurala K, Mallick S. Effect of annealing atmosphere on quaternary chalcogenide-based counter electrodes in dye-sensitized solar cell performance: synthesis of Cu_2FeSnS_4 and Cu_2CdSnS_4 nanoparticles by thermal decomposition process. *RSC Adv*, 2017, 7:15139–15148. https://doi.org/10.1039/c6ra28889h

[98] Hussein H, Yazdani A. Investigation the influence of Fe (III) doping in Cu_2ZnSnS_4 semiconductor: structural, optical and magnetic properties. *Optik*, 2019, 179:505–513. https://doi.org/10.1016/j.ijleo.2018.10.138

[99] Nefzi C, Souli M, Cuminal Y, *et al*. Effect of sulfur concentration on structural, optical and electrical properties of Cu_2FeSnS_4 thin films for solar cells and photocatalysis applications. *Superlattices Microstruct*, 2018, 124:17–29. https://doi.org/10.1016/j.spmi.2018.09.033

[100] Nefzi C, Souli M, Cuminal Y, *et al*. Effect of substrate temperature on physical properties of Cu_2FeSnS_4 thin films for photocatalysis applications. *Mater Sci Eng B*, 2020, 254:114509. https://doi.org/10.1016/j.mseb.2020.114509

[101] El Radaf IM, Al-Zahrani HY, Fouad SS, *et al*. Profound optical analysis for novel amorphous Cu_2FeSnS_4 thin films as an

absorber layer for thin film solar cells. *Ceram Int*, 2020, 46:18778–18784. https://doi.org/10.1016/j.ceramint.2020.04.195

[102] Babu GS, Shajan XS, George A, *et al*. Low-cost hydrothermal synthesis and characterization of pentanary $Cu_2Zn_xNi_{1-x}SnS_4$ nanoparticle inks for thin film solar cell applications. *Mater Sci Semicond Process*, 2017, 63:127–136. https://doi.org/10.1016/j.mssp.2017.02.015

[103] Rondiya S, Wadnerkar N, Jadhav Y, *et al*. Structural, electronic, and optical properties of Cu_2NiSnS_4: a combined experimental and theoretical study toward photovoltaic applications. *Chem Mater*, 2017, 29:3133–3142. https://doi.org/10.1021/acs.chemmater.7b00149

[104] Ghediya PR, Palan YM, Bhangadiya DP, *et al*. Electrical properties of Ag/p-Cu_2NiSnS_4 thin film Schottky diode. *Mater Today Commun*, 2021, 28:102697. https://doi.org/10.1016/j.mtcomm.2021.102697

[105] Babichuk IS, Yukhymchuk VO, Semenenko MO, *et al*. Optical and morphological properties of tetragonal Cu_2ZnSnS_4 thin films grown from sulphide precursors at lower temperatures. *Semicond Phys Quantum Electron Optoelectron*, 2014, 17:284–290. https://doi.org/10.15407/spqeo17.03.284

[106] Isacfranklin M, Yuvakkumar R, Ravi G, *et al*. Marigold flower like structured Cu_2NiSnS_4 electrode for high energy asymmetric solid state supercapacitors. *Sci Rep*, 2020, 10:19198. https://doi.org/10.1038/s41598-020-75879-9

[107] Sarkar S, Das B, Midya PR, *et al*. Optical and thermoelectric properties of chalcogenide based Cu_2NiSnS_4 nanoparticles synthesized by a novel hydrothermal route. *Mater Lett*, 2015, 152:155–158. https://doi.org/10.1016/j.matlet.2015.03.083

[108] Lu S, Yang H, Li F, *et al*. Element substitution of kesterite Cu_2ZnSnS_4 for efficient counter electrode of dye-sensitized solar cells. *Sci Rep*, 2018, 8:8714. https://doi.org/10.1038/s41598-018-26770-1

[109] Elyaagoubi M, Welatta F, Nkhaili L, *et al*. Development of Cu_2NiSnS_4 based thin film solar cells without a sulfurization step. *Mater Sci Semicond Process*, 2020, 107:104811. https://doi.org/10.1016/j.mssp.2019.104811

[110] Rajavedhanayagam J, Murugadoss V, Maurya DK, *et al*. Cu_2NiSnS_4/graphene nanohybrid as a newer counter electrode to boost-up the photoconversion efficiency of dye sensitized solar cell. *ES Energy Environ*, 2022, 18:65–74. https://doi.org/10.30919/esee8c753